
Radiation Damage In Scientific Charge-Coupled Devices

Master's Thesis

Niels Bassler

Institute of Physics and Astronomy
University of Aarhus
DK-8000 Aarhus C

31 August 2002



Radiation Damage In Scientific Charge-Coupled Devices

Master's Thesis

Niels Bassler

Institute of Physics and Astronomy
University of Aarhus
DK-8000 Aarhus C

31 August 2002



“Der Weg ist das Ziel.”

Contents

0.1	Preface	1
0.2	Acknowledgements	2
I	Background	3
1	Radiation in Space	5
1.1	Introduction	5
1.2	The Radiation Environment in Space	6
1.3	Expected Radiation Levels	10
2	CCD Parameters Affected by Radiation	15
2.1	Introduction	15
2.2	Types of Radiation Damage in Semiconductors	16
2.3	Key CCD Performance Parameters	22
2.4	Key Parameters in a Nutshell	29
II	CCD Radiation Testing	31
3	Experimental Work	33
3.1	Test Plan	33
3.2	CCD Characterization	33
3.3	Experimental Setup	38
4	Gamma Irradiation	43
4.1	Experimental Setup	43
4.2	Dosimetry	44
4.3	CCD Pre-Radiation Results	45
4.4	Total Dose Results	51
5	Proton Irradiation	59
5.1	Experimental Setup	59
5.2	CCD Pre-Radiation Results	63
5.3	Proton Irradiation Results	65
6	Annealing	69
6.1	Motivation	69
6.2	Investigations	69
6.3	Example	71

7 Discussion	75
7.1 Results	75
7.2 Conclusion	76
7.3 Outlook	77
III Appendices	81
A Tables with Stopping Powers and Ranges	83
A.1 Protons on Aluminium	83
A.2 Protons on Tantalum	85
A.3 Protons on Silicon	87
A.4 Electrons on Aluminium	89
B	91
B.1 CCD Voltages	91
B.2 CCD Timing	91
B.3 NIEL Data	92
B.4 Program Examples	93
B.5 Abbreviations	98

0.1 Preface

Charge-coupled devices (CCDs) were invented in the 1970, and have been under ongoing development since then. These ultra-low-noise and highly sensitive imaging devices have been the preferred detectors of astronomers since then, and exist in many different versions to suit the needs of various astronomical purposes. CCDs are commonly flown in space, for instance as the main detection instrument on several well known missions such as the Hubble Space Telescope, the Cassini Probe or XMM-Newton. Furthermore CCDs are also frequently used as the detection device in satellite Star Trackers, which provide attitude information to the satellite orientation system.

However, one major drawback is their extreme vulnerability to radiation, which is readily abundant in space. Needless to say that it is very important to investigate this, before a CCD is procured for a satellite mission.

Despite all modeling which have been performed on CCDs and testing on similar components, the only way to assess the reliability of a particular CCD in space, is to perform actual testing under conditions as close to those expected during the actual mission as possible. The experience in modeling gained in past years can be used to decrease the number of tests needed to qualify a component for space use.

The RØMER satellite holds the MONS instrument, a 32 cm space telescope, which will be used to detect stellar oscillations in nearby stars. The detection device is the backside illuminated CCD 47-20 from Marconi Applied Technologies. This thesis will focus on the impact of space radiation on this CCD. This device is also planned for use in the RØMER field monitor, and the front-side illuminated version will be used in the two star trackers on board the satellite.

Before I started with this task, I did not know much about the radiation environment and radiation damage in CCDs. But I could examine previous work described in various papers, and in addition my work at TERMA A/S in the same period was closely related to this thesis, which also helped a lot.

I put up a plan for the radiation tests:

1. Firstly, I had to investigate the radiation environment in space.
2. Then I examined from previous work done on different CCDs, what theories and observed problems are known with respect to radiation damage.
3. After this, I identified key parameters which would be affected with respect to the MONS mission.
4. Next, I designed and build in cooperation with the IFA workshop an experimental setup.
5. After a half year the setup was build, and the unavoidable problems which no one thought of before, had to be solved. Approximately one year after I started on my masters thesis, I was ready to perform the actual irradiation.

6. And at last, what I had to do, was data reduction and finish the writing of this thesis.

0.2 Acknowledgements

This thesis would not have been possible without the assistance from several fine people to whom I oblige my gratitude.

Very special thanks are given to Søren Frandsen for supervising me, Bjarne Thomsen for giving very useful advice and Hans Kjeldsen for his faith in the idea of doing irradiation tests at IFA and his limitless support.

I also thank the department of Medical Physics at Aarhus Kommunehospital, especially Anders Traberg for providing quick and smooth access to their accelerator and dosimetry facilities for the γ -ray irradiation.

I thank Niels Hertel and Jørgen S. Nielsen from ISA for providing access to the ASTRID synchrotron.

All these people have in common that they all have been very positive and open-minded towards this project, and gave lots of support.

Anton Norup Sørensen, IJAF, should also be mentioned here for his support with the IDL program for CTE determination.

Finally my friends Marcel Garbow and Philipp Gerhardy should be thanked for giving a helping hand during the actual irradiation.

Niels Bassler

University of Aarhus, Denmark, 31 August 2002.

Part I

Background

Chapter I

Radiation in Space

1.1 Introduction

Satellite electronics based on semiconductor technology suffer from the harsh radiation environment in space. In order to assure reliability of the satellite electronics, it is necessary to investigate the radiation environment encountered in space first, and determine the particle fluence (i.e. the number of particles encountered during mission time).

The radiation environment in space consists mainly of protons and electrons, with energies which are able to cause ionizing damage and displacement damage in the semiconductor material. Electrons and protons trapped in the magnetic field of the Earth contribute significantly to the total particle fluence experienced. The standard NASA AE-8 and AP-8 environment models are commonly used to determine trapped electron and trapped proton fluences, respectively.

In addition, solar flares may be encountered during mission lifetime, contributing significantly to the received dose. These radiation fluxes (i.e. number of particles per second) are of transient behaviour compared to the trapped particles, and their energy depends on the solar cycle. The JPL-91 model is normally used for determining this.

The particle fluence experienced by the satellite is highly dependent on the orbit, since the magnetic field of the Earth partially shields from solar flare radiation at equator, and partially increases particle flux at the polar regions. Trapped protons and electrons are encountered in large numbers in the Van Allen belts which are toroidal formed bodies encircling the Earth at equator as shown in figure 1.1.

The spatial distribution of the radiation fluxes is only to crude approximations symmetric; important asymmetries exist such as the infamous South Atlantic Anomaly.

Cosmic radiation originating from far outside our solar system has a very much lower flux than the trapped and solar particles. The nature of these particles is quite different from the others, which will be discussed in section 1.2.3. Thus, radiation encountered in space can roughly be classified into three groups:

1. Trapped radiation
2. Solar flares
3. Cosmic rays

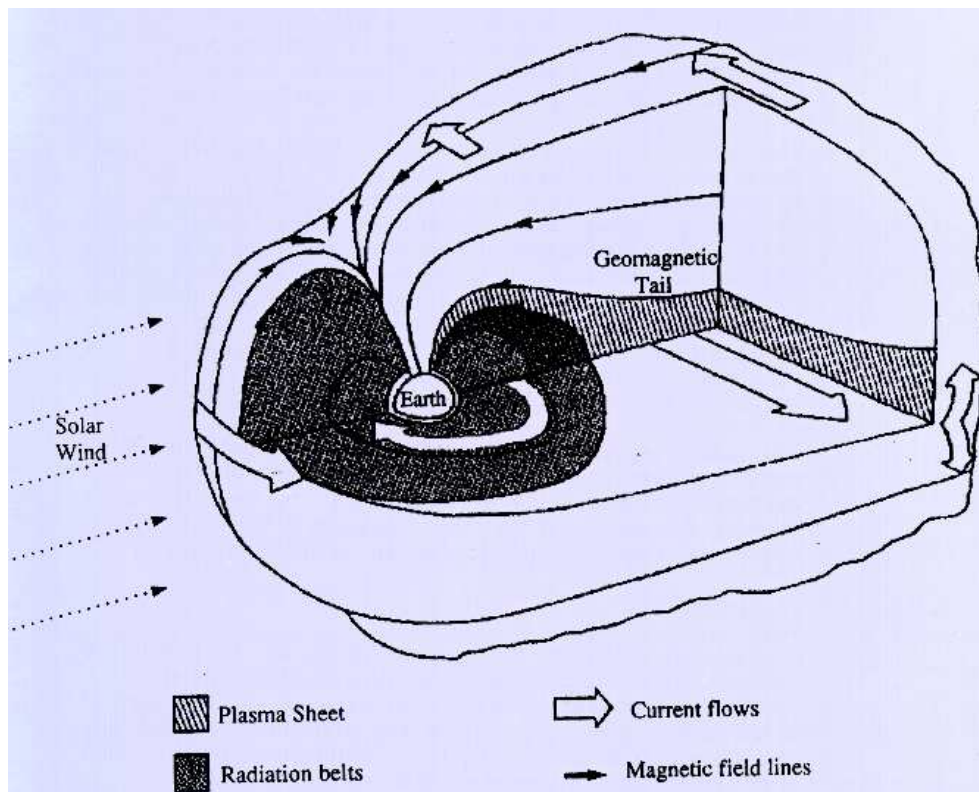


Figure 1.1 Illustration of the Van Allen radiation belts. *Source: [2].*

The next sections will briefly present the nature of these groups, and mention the problem with secondary radiation.

The CCD situated in the MONS telescope is expected to be one of the most vulnerable components in the RØMER satellite with respect to radiation, among the reaction wheels, the field monitor and the two star tracker CCDs. Since CCDs are most vulnerable to protons (e.g. reference [1]), special attention has been paid to this issue.

1.2 The Radiation Environment in Space

The following sections give a brief overview of the radiation encountered in space. A more elaborate version is given in “The Radiation Design Handbook” [2].

1.2.1 Trapped Particles

Trapped particles refer to electrons and protons trapped by the magnetic field of the Earth, formed as the toroidal shaped Van Allen Belts. Electrons reach energies up to 7 MeV, and protons may reach 300 MeV or more, becoming quickly less abundant at the higher energies. These particles usually originate from the sun,

but artificial sources such as nuclear weapons are also possible¹. The effects of nuclear weapons are also described in [2]. Since the trapped particle fluxes are dependent on solar activity, these may vary significantly on short time scale, which may cause problems on short-term type operations of e.g. astronomical character, e.g. if the CCD is saturated with signal from trapped protons when passing the radiation belts.

Electrons and protons become less penetrating for lower energies, so these can readily be absorbed by appropriate shielding. 1 cm of tantalum effectively blocks off all protons below 100 MeV as seen in the table in section A.2. Tantalum shields have been utilized on board e.g. the Hubble Space Telescope and the Galileo Mission.

Standard models describing the trapped particle environment have been developed, NASA's popular AE-8 MIN and AP-8 MIN models for determining electron and proton flux for solar minimum have been applied in all trapped particle calculation in this thesis.

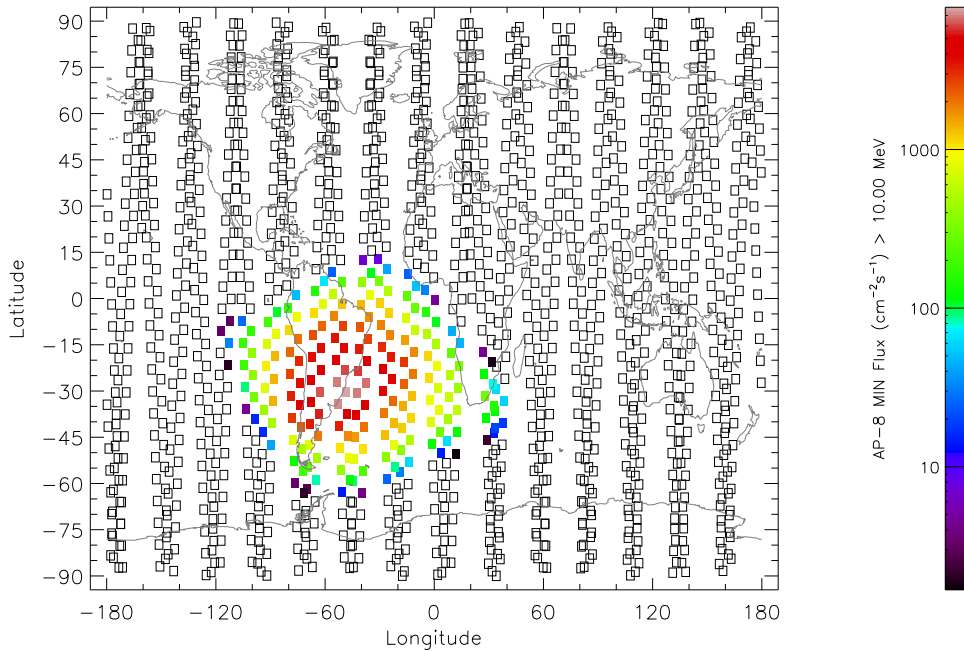


Figure 1.2 Proton flux for a low Earth orbit in an altitude of 894 km during solar maximum. The South Atlantic Anomaly is clearly visible. Note that only protons with energies above 10 MeV are taken into account here. Lower proton energies are also encountered at the polar regions.

1.2.2 Solar Flares

Solar flares are readily encountered during solar active periods. These contribute with a transient proton flux of variable intensity. The spectrum is more soft than

¹The American “Starfish” nuclear detonation in 1962 contributed with a severe amount of trapped electrons, which persisted several years.

the trapped proton spectrum. Solar flares are the main source of radiation for satellites in the geosynchronous orbit and for satellites in the global positioning system (GPS) orbit, which are positioned well above the radiation belts of the Earth. Low orbiting satellites may be shielded from solar protons by the magnetic field close to the equator, but will experience a higher flux near the polar region, where solar flare protons tend to funnel. Geomagnetic storms may significantly alter this shielding effect, though.

All solar flare calculations in this thesis were done with the JPL-91 model.

1.2.3 Cosmic Rays

Cosmic radiation originates from the galactic center, and consists of electrons and all types of nuclei with element numbers ranging from $1 \leq Z \leq 92$ (hydrogen to uranium). Energies range from some MeV per nucleon to several GeV per nucleon - and rarely even to energies in the order of TeV per nucleon. The ionizing effect of these ions is dependent on their energy and mass². The effect of these ions is quantized in terms of their linear energy transfer (LET $MeV/mg/cm^2$), almost equivalent to the electronic stopping power. The radiation hardness of a semiconductor device can be verified with this parameter only. This eases testing significantly, since one can create different LETs by solely varying the energy of a specific particle type instead of testing for all 92 particle types.

Cosmic rays are, in contradiction to the trapped and solar protons, treated as single events, since these are much less abundant. The contribution of cosmic rays to the total ionizing dose received by the satellite is negligible. However, considering their high energy and (occasionally high) mass, it makes digital devices very vulnerable. Cosmic rays are capable of introducing errors such as bit-flips, latch-ups and the fatal burn-outs. To quantize these effects, LET is used as a threshold, when exceeded the component is likely to suffer from one of the above stated errors.

It is very difficult to protect from cosmic rays, since this implies mounting vast amounts of shielding which is not feasible on a satellite. Instead radiation hardened semiconductors are designed and error detecting/correcting code is used, such as Hamming or Reed-Solomon³. Also redundant design is usually applied, to achieve a higher fault tolerance.

1.2.4 Secondary Radiation

Secondary radiation is generated, when any of the above stated radiation types interact with the satellite structure. Usually the sensitive electronic devices are shielded in some way, to prolong their lifetime and inhibit degradation. Especially electrons stopped in shielding generate bremsstrahlung, which is a continuous spectrum of gamma and x-rays with energies below the incident electron energy.

²The ionizing effect is independent on charge though. When ions enter a material their charge state will quickly reach a state of equilibrium, independent on their initial amount of charging.

³Reed-Solomon error correcting code is used on audio compact disks.

Also secondary protons and neutrons⁴ may be generated, preferably in shields consisting of a material with higher nuclear mass, such as tantalum. To avoid this, shields of aluminium are preferred, since these effectively stop electrons and low energy protons. Tantalum shields are used for shielding CCDs in the Hubble Space Telescope and the Galileo mission, but the increased nuclear mass of tantalum results in a significant neutron flux, which is problematic for delicate devices such as CCDs. Tantalum shields are more effective for the same aluminium thickness, but in the end aluminium is the more effective shield type per gram, which is shown in [3]. See also the tables in appendix A. Unless any sterical problems exist, aluminium should be the preferred, as it is for the MONS telescope.

At last it should be noted that the satellite structure itself is getting activated, primarily due to the proton bombardment, but this is generally considered to have a negligible effect compared with the natural occurring particle fluxes in space.

⁴Neutrons at high energies are basically behaving just as protons, since the coulomb-barrier interacting with the proton is easily penetrated.

1.3 Expected Radiation Levels

Using the SPENVIS [4] online software, expected radiation doses for the RØMER Molniya orbit has been calculated.

1.3.1 The Molniya Orbit

The baseline RØMER Molniya orbit parameters were provided by The Danish Space Research Institute (DSRI). The SPENVIS software calculated satellite positions for 229 positions during two days beginning at the orbit epoch. The location of these discrete positions are shown in figure 1.3. The launch date was not defined at the time when writing this thesis, but the baseline aimed at a launch sometime in August 2005.

Orbit description:

Orbit epoch:	31. Aug. 2005 00:00:00
Altitude at Perigee:	600 <i>km</i>
Altitude at Apogee:	39767 <i>km</i>
Inclination:	63.435°
RA of ascending node:	173°
Argument of Perigee:	270°
True anomaly:	0.00000°
Eccentricity:	0.73748
Semi latus rectum:	12111.99601 <i>km</i>
Semi major axis:	26554.50000 <i>km</i>
Mean motion:	12.60599 <i>rad/day</i>

The Molniya orbit was chosen for the RØMER mission for several reasons. First of all, the satellite reaction wheels which control the attitude, have to dump momentum. Electric coils are equipped on the satellite, which can interact with the earths magnetic field, when the satellite passes at perigee. The high inclination of the Molniya orbit provides the possibility to dump momentum for all three vectors, which would not have been possible when selecting a geo transfer orbit launched from equator with an inclination of 0°.

Furthermore, due to the eccentric nature of the orbit, the Earth is only obscuring targets in a limited amount of time. This enables long uninterrupted data series, which are desirable for the astereoseismology group.

In addition, this orbit was visible from Denmark every 2. orbit, which eases downlink of data. At last, the Soyus Fregat from STARSEM at the Baikonur Cosmodrome is a relatively cheap launcher.

1.3.2 Radiation Environment Analysis

The RØMER satellite in the Molniya orbit passes the Van Allen belts 4 times a day, where the satellite will experience high fluences of trapped protons and electrons. The electrons are readily stopped and converted into bremsstrahlung. The

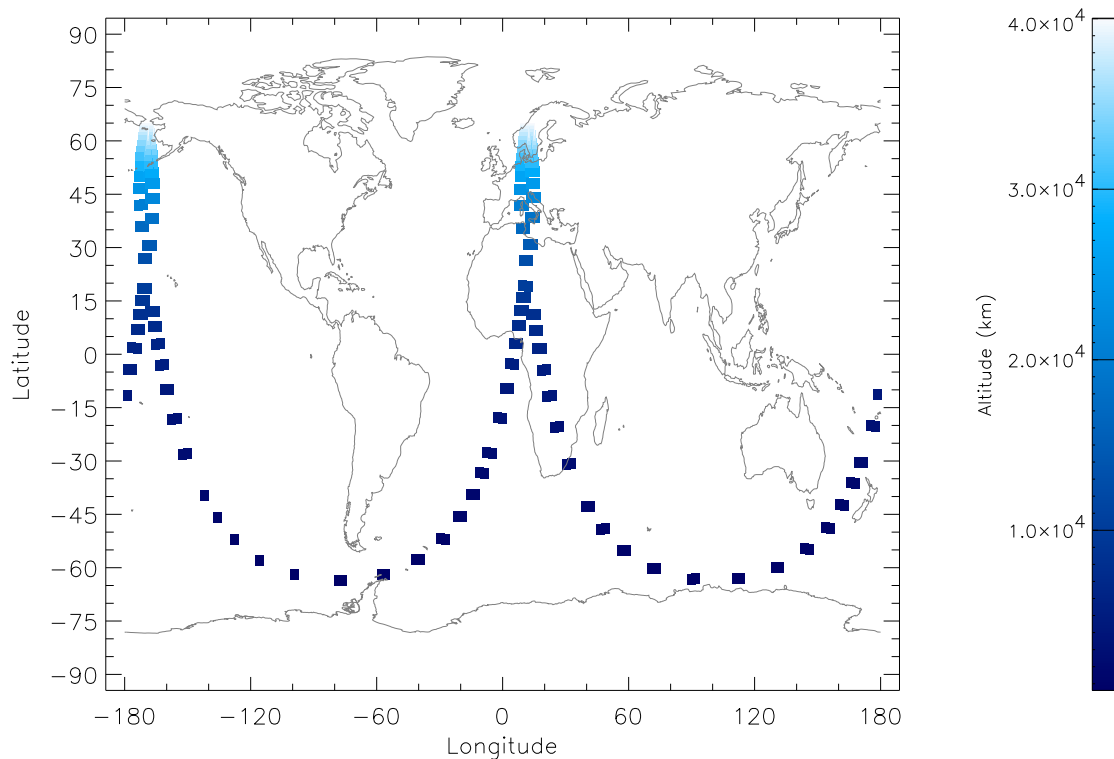


Figure 1.3 Illustration of the RØMER Molniya orbit.

RØMER baseline implies 20 mm of Aluminium shielding. This effectively stops all electrons, and primary protons up to approximately 70 MeV (see table A.1 in appendix A).

For the radiation analysis the following models were applicated:

- Trapped particles: AP8-MIN, AE8-MIN (Confidence level 50%, local time variation not included)
- Solar flares: JPL-91 (Geomagnetic shielding included, quiet magneto-sphere conditions, mission duration 2 years, confidence level is 95% not to exceed fluxes)

The RØMER mission is planned to last 2 years.

Total dose calculations

Total dose calculation were performed by the SPENVIS software, utilizing the SHIELDOSE-2 model. Silicon was selected as the target material. The results are presented in table 1.1.

It is evident that most ionizing damage is originating from the trapped protons, other contributions are minor.

Table 1.1 Total ionizing dose contributions from various particle sources, after 20 mm of aluminium shielding.

Source	Dose, kRad(Si)
Electrons	0.000
Bremsstrahlung	0.106
Trapped protons	1.301
Solar protons	0.152
TOTAL:	1.559

Total Proton Fluence

The entire proton fluence is mainly originating from the trapped protons in the Van Allen Belts. The critical parameters for the CCD (MONS telescope as well as in the Star Trackers) scale linearly with the non-ionizing energy loss of protons, therefore the “10 MeV damage equivalent protons” term is applied here. This term is a way of describing the amount of displacement damage the radiation causes, and will be explained in detail in chapter 2. In figure 1.4, the 10 MeV equivalent proton fluence is plotted versus the shielding thickness.

At 20 mm of spherical 4π shielding, the total mission fluence is $4.97 \cdot 10^9 \text{ protons/cm}^2$. If only 10 mm of shielding would be applied, the dose would be about twice as high: $1.06 \cdot 10^{10} \text{ protons/cm}^2$.

Radiation Dose Summary

The total dose, the MONS CCD will experience post 20 mm of shielding during two years is restated in the box below.

Total ionizing dose:	1.56 kRad(Si)
Total non-ionizing dose:	$4.97 \cdot 10^9 \text{ protons/cm}^2$ (10 MeV equivalent protons)

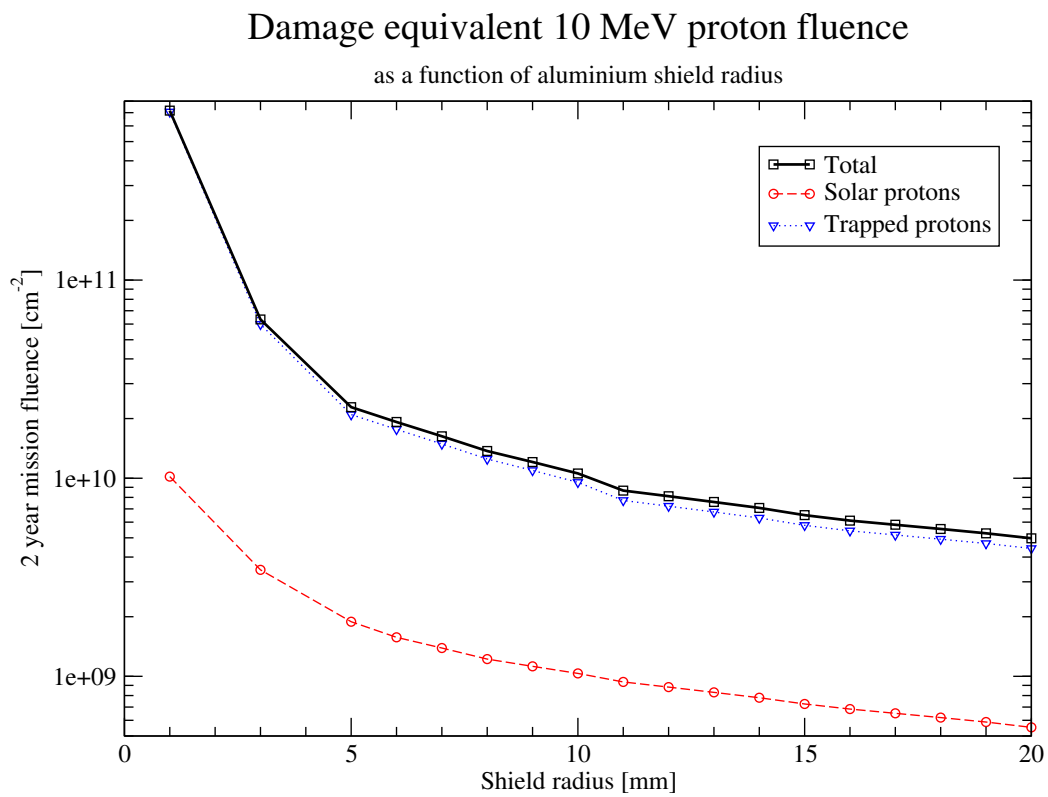


Figure 1.4 Damage equivalent 10 MeV proton 2-year mission fluence for the RØMER Molniya Orbit.

Chapter II

CCD Parameters Affected by Radiation

2.1 Introduction

Charge coupled devices (CCDs) are very sensitive to radiation, compared to other semiconductors. The main problem arises when CCDs are used in long-term space missions, where naturally occurring radiation will degrade the component. Several properties are affected, and will now be discussed in detail.

Behind 20 mm of aluminium shielding as for the CCD on the MONS telescope, only protons and bremsstrahlung are encountered, almost all electrons are converted to bremsstrahlung (i.e. γ -rays and X-rays). A minor fraction of the protons is converted to secondary neutrons as well, becoming more significant for shielding with higher Z .

20 years ago it was still assumed that 1 kRad total ionizing dose of ^{60}Co radiation was damage equivalent to 1 kRad total ionizing dose of proton damage. This proved to be wrong, a CCD which easily could withstand 20 kRads(Si) of ^{60}Co gamma rays, suffered significant charge transfer efficiency (CTE) losses at 1 kRad(Si) of proton damage [3]. It was then realized that the CTE degradation is associated with the non-ionizing energy loss (NIEL), caused by displacement damage in the bulk silicon material, which is far larger for low energy protons (less than 10 MeV) than for γ -rays.

All results presented in this chapter are based on previous testing of various CCDs. Some of these results are very dependent on the design of the CCD, and cannot directly be applied for a particular CCD such as the Marconi CCD 47-20. The purpose of presenting these results are solely to give a feeling for the magnitudes of the radiation effects.

2.2 Types of Radiation Damage in Semiconductors

The actual damage caused by protons and bremsstrahlung is categorized into two groups:

- Ionization damage
- Displacement damage

The figure 2.1 gives an overview of the radiation damage issue on CCDs, and is now described in detail in the next sections.

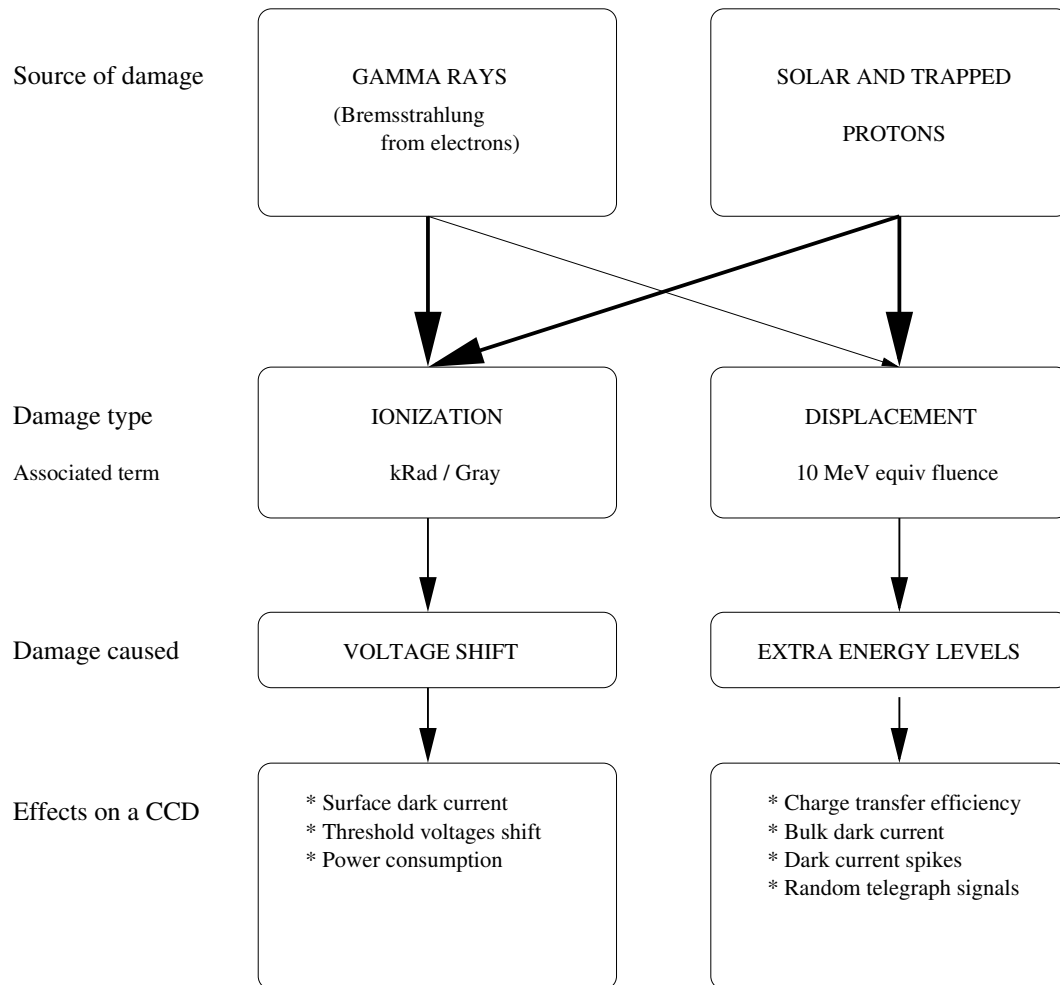


Figure 2.1 The radiation damage tree for CCDs.

2.2.1 CCD structure

A general overview of the way the CCD works is given in [5]. A typical standard CCD pixel element consists of a p+ substrate layer, whereupon an epitaxial p

layer is grown. Upon this layer a thin silicon-oxide layer is grown. A polycrystalline gate structure connects the pixel with the three clocking phases.

The charge collecting pixel of the CCD can be illustrated with a potential well, which holds the electrons generated by incoming photons. For the CCD described above, the charge collecting region is just at the interface between the silicon-oxide layer and the epitaxial layer. This is unfortunate, since this interface state is the source of large amounts of surface dark current.

Instead, phosphorous is implanted into the p-layer, converting it to a n type carrier with an excess of holes. This modifies the potential well, so the charge collecting region is moved below the silicon-oxide interface state. This is illustrated in figure 2.2.

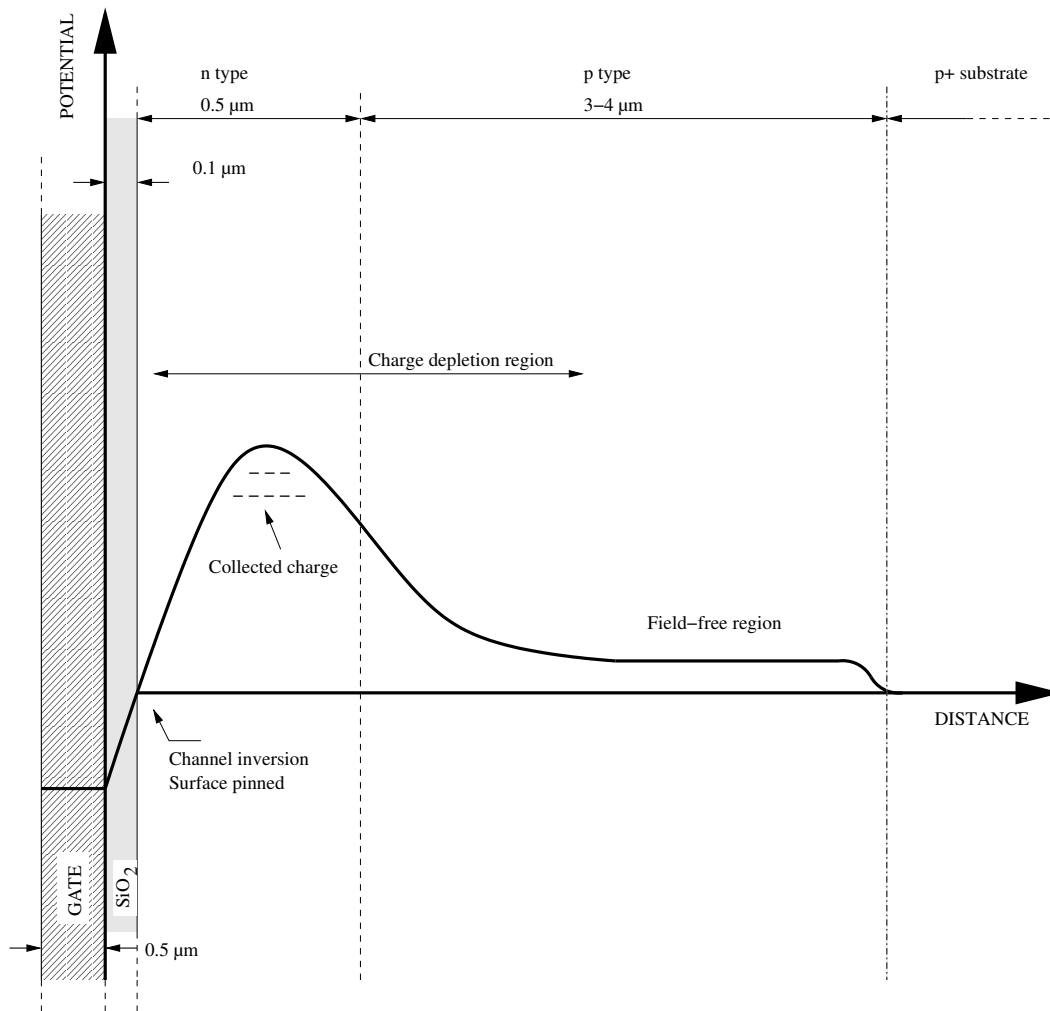


Figure 2.2 Cross-section of a single pixel element of a buried channel CCD. The potential curve illustrates the depletion layer, and the field free region. (The dimensions stated here are typical, and may vary.)

2.2.2 Ionization Damage

Both protons and bremsstrahlung will lose most of their energy by ionization of the target material. This will have various effects on the silicon material, but mainly it will introduce electron hole pairs throughout the material. The CCD 47-20 is suspected to consist of an oxide and/or nitride layer, a n-type channel implanted upon a p-type epitaxial layer, which is grown on the bulk material, which will be some low resistivity material such as p+ doped silicon. The actual charge depletion will happen partially in the p-layer and n-channel, but the n-channel is used to move the charge out of the pixel element.

CCDs (and other MOS devices) will accumulate charge in the gate oxide thereby changing the threshold voltages. The principle of this damage mechanism is sketched in figure 2.3. Ionizing radiation generates electron-hole pairs within the oxide structure. If no electric field is applied, then these electron-hole pairs are most likely to recombine again with no further implications. But when a gate voltage generates an electric field, the electrons will quickly leave the structure. If the gate voltage is positive with respect to the silicon substrate, they will travel through the gate. The remaining holes have a significantly lower mobility than the electrons, since the transportation mechanism is different¹. A fraction of these hole will then be trapped at the interface layer, and may reside there up to several years. This causes a negative shift of the threshold voltage. The term “threshold voltage” is derived from MOS-FETs, where a certain gate voltage is required to trigger the transistor due to this effect.

In addition MOS switches may not fully close anymore, due to the extra electric field within the oxide layer, and this leads to an increased power consumption of the device.

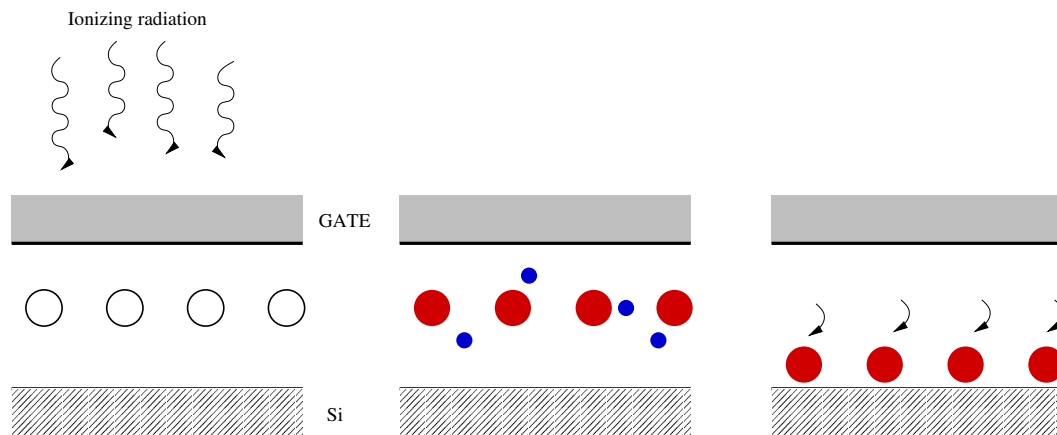


Figure 2.3 When ionizing damage hits the SiO_2 structure electron-hole pairs are generated. For positive gate values the electrons leave the oxide layer through gate terminal. The holes move more slowly towards the silicon interface, where they are very likely to be trapped and generate an electric field within the structure, which may persist several years.

For a CCD this will affect the clocking voltages and the reset voltage V_{DR} .

¹Described as a stochastic hopping transport through localized states in the oxide layer.

Furthermore, dark current will increase at the SiO_2/Si interface, since ionizing radiation also increases the amount of trapping states located here. But since the CCD 47-20 is a buried channel CCD, the depletion layer is pulled away from the interface. This effect is reduced even more when the CCD is operated in inverted mode, as it is with the MONS CCD. In the inverted mode, the phase is adjusted so the substrate and surface potential become equal - which actually is shown in figure 2.2. By this way holes are attracted and “pinned” at the surface, the amount increasing as the phase is driven more negatively, maintaining a potential of zero volts, relative to the substrate. These holes limit the surface dark current generation.

In fact, the Marconi CCD 47-20 is a *Multi-Phase Pinned* (MPP) device, meaning all phases are operated inverted during integration. This would cause the charge to bloom across several pixels, if this would be done with an ordinary CCD. MPP technology omits this by doping one of the three phases with boron, thereby neutralizing the n-channel. This is then the collecting phase.

2.2.3 Displacement Damage

Especially low energy protons will interact with the silicon atoms by coulomb forces, and thus loose energy by causing displacement damage to the lattice. This can be visualized as a nucleon, which has left its original position in an elsewhere perfect crystal lattice. This energy loss due to displacement damage, is referred to as non-ionizing energy loss (NIEL), and is directly correlated with the CTE degradation, as described in section 2.3.3.

This NIEL can be divided into two groups, elastic and inelastic NIEL, where nuclear reactions account for the inelastic part of the NIEL, and displacement damage for the elastic part. The latter is the most prominent effect observed. Compton electrons produced through elastic scattering of gamma rays from a ^{60}Co source (1.25 MeV γ -rays) with atomic electrons, have typically an energy of 580 keV and may collide with silicon atom, creating a vacancy [7] in the semiconductor lattice. In general, photons with energies larger than 400 keV may cause displacement damage (see [8]) in the lattice as well.

For a n-type buried channel CCD such as the Marconi CCD 47-20, the most likely result is the generation of phosphorous-vacancy centers which will introduce an extra energy level between the conduction band and valence band of the semiconductor material. This will result in charge trapping, which will lead to CTE degradation and an increase in the bulk dark current. The effect of an extra energy level between the conduction and valence band is shown in figure 2.4. The worst defects are those defects, which reside in the middle of the energy gap, since it is - popular spoken - more likely for an electron to receive two smaller amounts of energy, than one tiny and one large amount. This is the case for the phosphor-vacancy, as it is placed about 0.4 eV below the conduction band.

Charge trapping, as illustrated in figure 2.5, may also happen if the energy level associated with the defect is empty. Charge passing a pixel with a defect, can be trapped in the energy band, and may have a chance to be re-released some

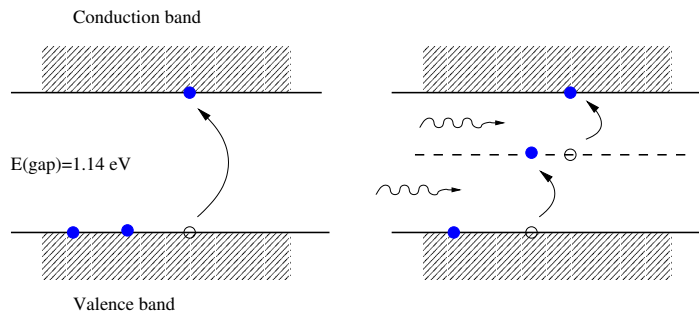


Figure 2.4 In a perfect semiconductor, the energy required to raise an electron from the valence band to the conduction band is 1.14 eV. If the temperature is low enough, only few electrons from the valence have this energy, and this results in a low dark current. If however an extra energy level is introduced, electrons can reach the conduction band more easily by successively gaining smaller amounts of energy. On a CCD this is seen as an increased dark current.

time later, depending on the temperature, or proceeds to the valence band. For CCD operation it means that some charge may be deferred during read out, or eventually the information is lost forever if trapping time constant is longer than the clock-cycle of the CCD. If the trapping time constants are very long, typically at cryogenic temperatures, the “fat-zero” method can be applied. The CCD is then pre-flashed with light, in order to fill all the traps with charge, so no further charge is lost.

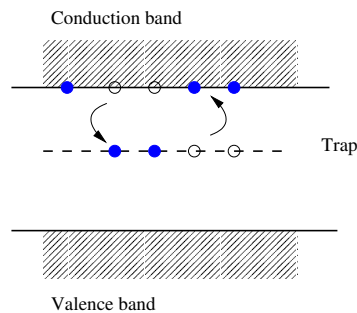


Figure 2.5 If the extra energy band is empty, it may trap some electrons, and release them again after a highly temperature dependent trapping time. For a CCD this is seen as poor CTE.

Since low energy protons are the main source for displacement effects in silicon material, it is not favoured to use the term “kRad(Si)” when dealing with protons doses. Instead the term fluence ($protons/cm^2$) should be used. In space, a whole spectrum of energies are associated with the encountered protons and photons, and just like the case for the ionizing damage, it is appropriate, to find a term, which describes the entire amount of displacement damage, the spectrum of protons will cause in the semiconductor. Since the NIEL is known for any particle energy, and the spectrum is known, the total NIEL for a mission can be calculated. This can then be transferred to a specific proton fluence of 10 MeV protons which create the same amount of displacement damage in the material of interest. Therefore the term “10 MeV equivalent protons” is used. The NIEL

as a function of proton energy is shown later in figure 2.8.

Still, these protons also produce ionizing damage as well, and this can be calculated by the electron stopping power:

$$D = 1.6 \cdot 10^{-8} \frac{\text{Rad} \cdot \text{g}}{\text{MeV}} \cdot \Phi \cdot \left(\frac{dE}{dx} \right) \quad (2.1)$$

where D is the ionizing dose in Rad, Φ is the fluence in $\text{protons}/\text{cm}^2$ and $\frac{dE}{dx}$ is the electron stopping power in $(\text{MeV} \text{ cm}^2/\text{g})$ (see section A). The factor $1.6 \cdot 10^{-8}$ is merely the conversion factor from MeV/g to Rad ($1 \text{ Rad} = 100 \text{ erg}/\text{g}$). Figure 2.6 illustrates this equation.

Note that this equation assumes a thin target. In thick targets, $\frac{dE}{dx}$ will vary as a function of depth.

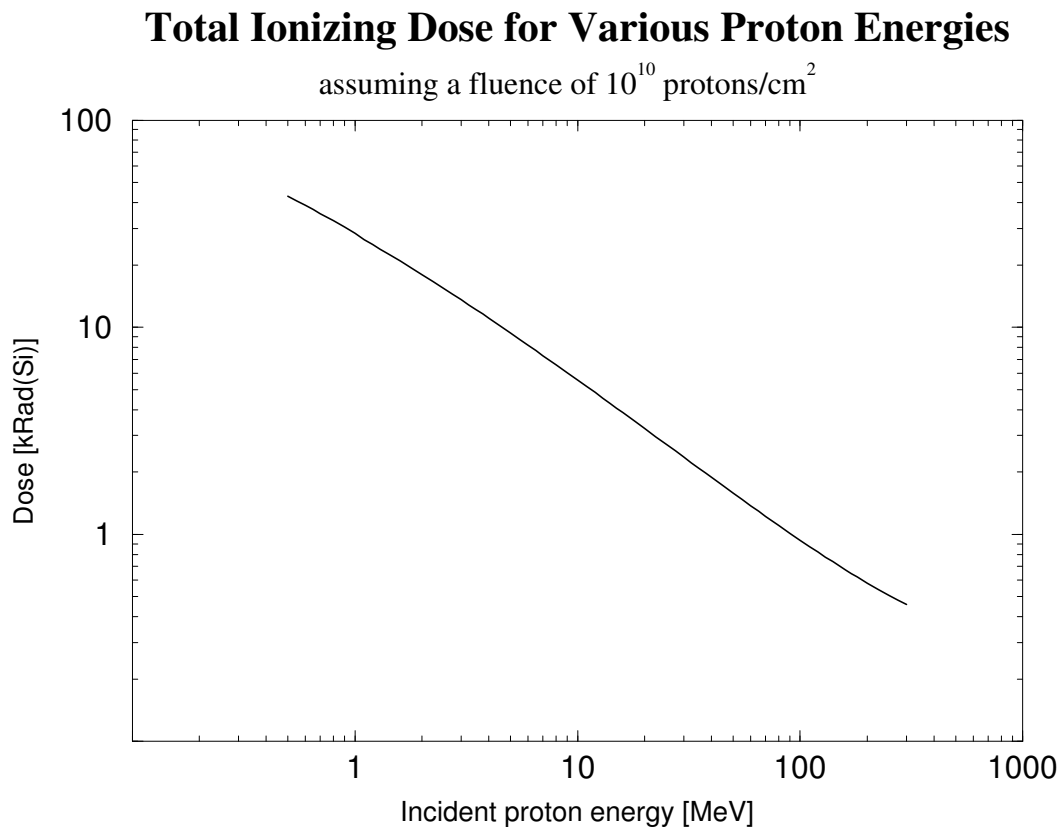


Figure 2.6 Total ionizing dose as a function of proton energy. The dose scales linearly with the fluence.

2.3 Key CCD Performance Parameters

The key parameters affected when a CCD-detector is exposed to radiation are:

- Dark Current
- Threshold Voltages
- Charge Transfer Efficiency (CTE)
- Linearity and full well capacity

Other parameters are affected as well, but may be less relevant in the context of the MONS telescope:

- Power consumption
- Readout noise
- Gain
- Spectral response

2.3.1 Power Consumption

Hopkinson [6] has done tests on some Thomson CCDs, where the power consumption of the output amplifier (I_{DD}) and the clock drivers (I_{DDA}) were monitored. The currents were monitored during ^{60}Co irradiation, and were found to increase linearly with dose by an amount independent of dose rate. A TH7863 CCD showed increase in I_{DD} of 0.12 mA/kRad when powered, and 0.04 mA/kRad when unpowered during irradiation.

2.3.2 Threshold Voltages

Radiation will influence the threshold voltages of the CCDs, since holes are likely to be trapped in deep traps at the oxide surface, and cause the gate potential of the MOS structure to shift.

Both the reset voltage threshold (V_{DR}) as well as the clocking voltage threshold will alter due to this effect. Hopkinson found for the TH7863 CCD a linear increase of the reset voltage threshold of $0.09 \text{ V/kRad}(Si)$ when irradiating with ^{60}Co during power on. This result is remarkably consistent with the results stated in the Marconi report [9]: here voltage shifts of $\sim 0.1 \text{ Volt/kRad}(Si)$ are found. When unpowered during irradiation, the shift in the reset voltage threshold was only 0.024 V at $15 \text{ kRad}(Si)$, according to Hopkinson. The Marconi report states 0.250 V at $10 \text{ kRad}(Si)$ when irradiating with ^{90}Sr β -rays.

No annealing effects were noticed after irradiation had ceased (Hopkinson).

It is very important to assess the operating window of the CCD voltages, and then choose the operating voltages in such a way that radiation encountered in space will not cause the component to fail, e.g. when the reset FET no longer is able to turn off, the CCD ceases to clock, or the CCD is taken out of inversion. The Marconi report provides a cookbook solution for how to select proper voltages.

The Marconi CCD 47-20 has no protection diodes, which makes it possible to operate the CCD in inverted mode, thus the clocking voltages can be operated over

a wide range, but nonetheless this is an issue, which should be investigated by device testing. The investigation of the flat band voltage shift, will be a central part of this thesis.

2.3.3 Charge Transfer Efficiency

As stated in the introduction, CTE degradation is directly related with NIEL. Low energy protons will readily cause displacement damage in the CCD, and for a n-type CCD the phosphor vacancy is favoured. The energy level of this defect is located $0.44 eV$ below the conduction band. This may cause valence electrons to thermally hop into the traps and be a source for dark current. Also the traps are able to hold charge for some time, highly depending on the operating temperature, and then release the deferred charge again. This is causing the degradation in CTE.

The time constant quickly becomes large for low temperatures, which is one reason why astronomers cool their CCDs; the CTE will significantly improve when the time constant of the traps is larger than the read out time. The traps will then quickly be filled if there is a signal when starting to read out the CCD, and then no further charge is lost during read out. Janesick [10] gives a detailed description of the CTE issue and also an equation for the emission time constant τ_e :

$$\tau_e = \frac{\exp(E_T/kT)}{X_n \sigma_n v_{th} N_C} \quad (2.2)$$

where E_T is the trap energy level below the conduction band in eV , k is Boltzmanns constant, T is the temperature in Kelvin, X_n is an entropy factor, σ_n is the electron cross-section and is related to the ability of the trap to trap an electron, measured in cm^2 . This value is in the order of atomic dimension, about $10^{-15} cm^2$. v_{th} is the thermal velocity of the electron, and is in the order of $10^7 cm/sec$ (see footnote²) and finally N_C is the effective number of states in the conduction band, $2.8 \cdot 10^{19} states/cm^3$.

For the phosphor vacancy, some typical emission times are listed in the table below and illustrated in the figure 2.7, assuming $X_{PV} \sigma_n = 5 \cdot 10^{-15} cm^2$, ($\sigma_n = 3.5 \cdot 10^{-15} cm^2$), $v_{th} N_C = 1.6 \cdot 10^{21} \cdot T^2$ and the $E_T = 0.44 eV$:

Temperature ($^{\circ}C$)	τ_e (sec)
+25	3e-5
-60	0.056
-80	0.83
-100	22
-120	1380

The CCD clocking times of the experimental setup in thesis, are stated in the appendix B.2.

It is now possible to calculate the amount of CTE degradation the CCD will suffer in space. The SPENVIS tool offers this feature. This is based on a predictive approach, in which it is known that the displacement damage effects in

² $v_{th} = (3kT/m_e^*) \sim 10^7$, where m_e^* is the effective electron mass.

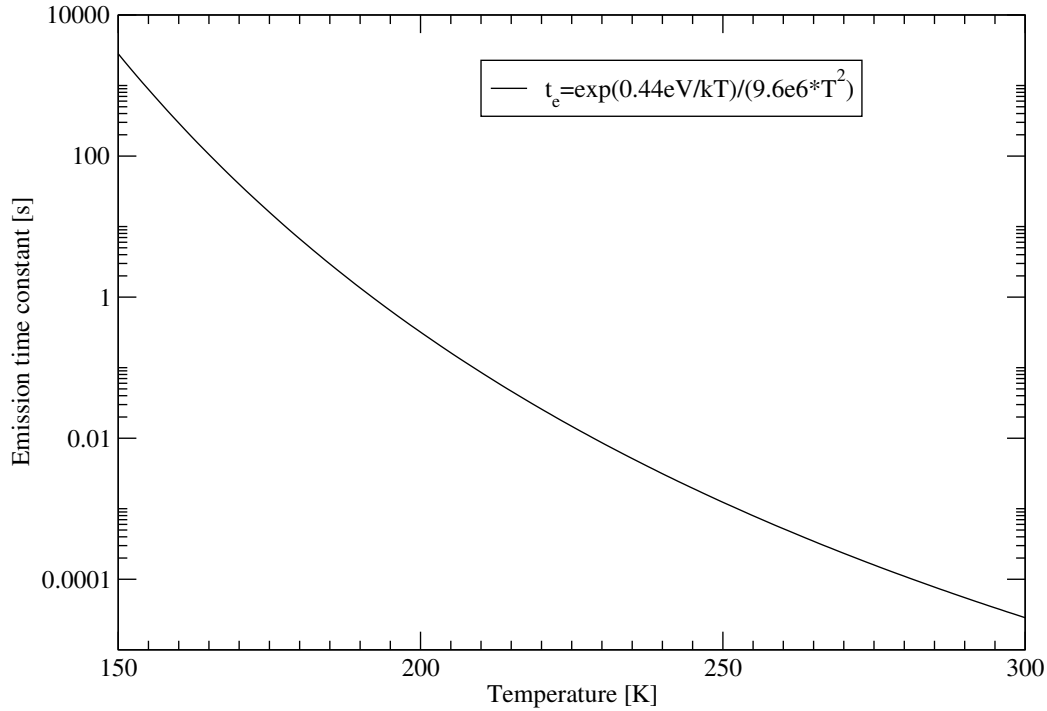


Figure 2.7 Emission time constants as a function of temperature for the phosphor vacancy, located 0.44 eV below the conduction band.

a device for a given energy can be correlated to other energies (and even other particles).

The relationship between NIEL and CTE degradation is illustrated in figure 2.8. The scale factor (which connects the CTE degradation with the NIEL) is a device specific constant, depending on the same parameters as CTE, and can be determined by performing irradiation tests.

CTE is very much depending on the time the CCD is clocked with, but also the signal level and the background level influence the CTE performance. Furthermore temperature is important to the trapping constants. In this thesis CTE was determined by the ^{55}Fe method solely, with no background (except for the dark current in the pictures at room temperature).

Note that ionizing damage may also have an indirect influence on CTE degradation, due to a shift in the clock operating voltages to the CCD, e.g. when the CCD is taken out of inversion.

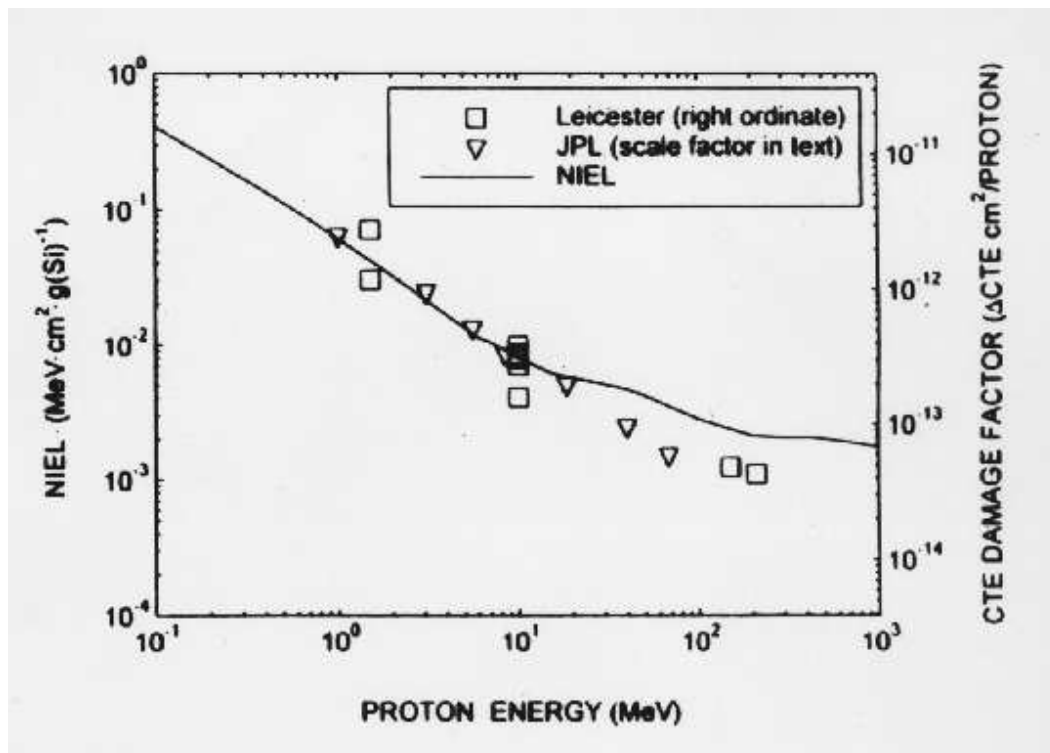


Figure 2.8 NIEL compared with CTE degradation. Scale factors are $3.9 \cdot 10^{-11}$ and $1.2 \cdot 10^{-11} \Delta CTE \cdot g(Si)/MeV$ for Leicester and JPL data respectively. Source: [3].

2.3.4 Localized “Bottomless” Traps

Localized traps, which are able to hold vast amounts of charge - seeming bottomless -, are seen as dead columns on the CCD. These columns start at the trap itself and continue in parallel, but opposite direction of the read out direction, and end at the edge of the CCD. White columns are due to another type of localized trap, in which charge is continuously released instead (i.e. a very hot pixel). Both traps are only significant at high temperatures, and become passive at low temperatures. These particular traps are caused by some impurities in the silicon material itself during manufacturing, and not by the moderate radiation levels encountered in space.

2.3.5 Dark Current

Dark Current will increase when CCDs are irradiated, and this is mainly a product of the ionizing damage in the CCD, but can also be caused by displacement damage. The origin of dark current is divided into two groups: 1) Surface dark current, 2) Bulk dark current.

Surface Dark Current

Surface Dark Current arises at the SiO_2/Si interface in CCDs (and other MOS devices), and will increase as a function of the ionizing dose, the component re-

ceives. For non-inverted CCDs this is the main contribution to dark current. When CCDs are operated in inverted mode, the surface dark current is effectively suppressed. According to [9], the surface generated dark current is close to the detection limit in inverted CCDs.

Ionizing radiation will not cause any significant increase of surface dark current, as long as the CCD is inverted, and the readout time is kept short.

Bulk Dark Current

Radiation, which create displacement damage in the depletion region of the CCD (mainly protons, but also γ -rays), introduces new defect states in the silicon band gap. As mentioned before, the major defect state is the phosphor-vacancy (P-V) for n-type buried channel CCDs, located 0.44 eV below the conduction band. Thermal electrons from this state may then enter the conduction band, resulting in a bulk dark current, as described in section 2.2.3.

As stated in [9], work on Marconi CCD 47 devices revealed that the increase in bulk dark current Δs scales with the NIEL, Temperature and received flux as:

$$\Delta s \approx 10^{-5} \cdot V \cdot \phi \cdot NIEL \cdot T^2 \cdot \exp\left(\frac{-6616}{T}\right) \quad (2.3)$$

Δs is in electrons per pixel per second (measured 3 months after irradiation), V is the depletion volume in μm^3 , ϕ is the proton fluence and NIEL is in $keV cm^2/g$. An example is shown in figure 2.9.

(The thickness of the depletion layer may be around 3 μm for the Marconi CCD 47-20 according to [11].

Dark Current Spikes / Defective Pixels

Due to the stochastic nature of the dark current distribution some pixels with particular high dark current can occur. These are also referred to as hot pixels. Previous testing on CCDs (e.g. [9] and [6]) revealed an increase in these pixels with increasing proton dose. Typical dark currents of the largest spikes observed were in the order of $\sim 3 nA/cm^2$ at approximately $+21^\circ C$.

Random Telegraph Signals

As stated in [9], proton irradiation cause some pixels to fluctuate in dark current, which is known as Random Telegraph Signals (RTS). The dark current will flip randomly between two or more discrete generation rates. The average time constant for each state are well defined. The Marconi report shows a way to predict these time constants, which was 6 days at $-30^\circ C$, and 10 seconds at $50^\circ C$. The amount of RTS defects in a pixel follows a Poisson distribution, and will increase as a function of proton fluence.

The Marconi report mentions that there are indications that this effect may be caused by elastic NIEL and not inelastic NIEL, which means that this effect is not a result of nuclear reactions (protons being intercepted by silicon atoms).

Since the MONS telescope will operate in cryogenic conditions, the RTS issue is

Mean Dark Signal Increase as a function of Temperature

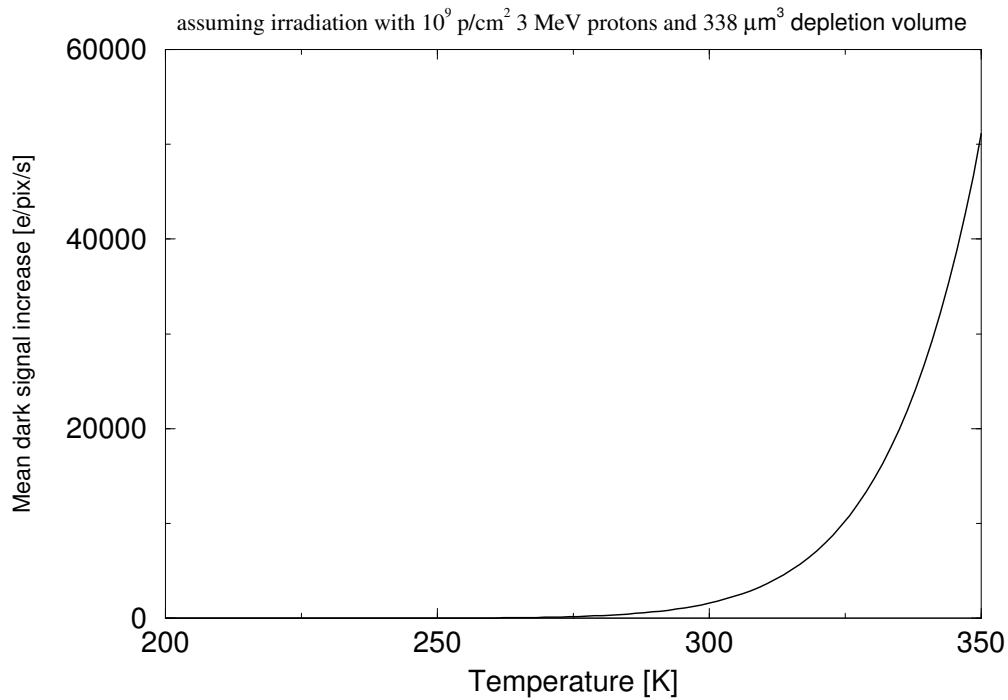


Figure 2.9 Δs vs. temperature after irradiation with 3 MeV protons.

considered insignificant.

2.3.6 Linearity and Full Well Capacity

Full well capacity (FWC) can be defined as the output signal, where the linearity still is better than 5%. According to Hopkinson's [6] tests on Thomson CCDs, full well capacity will slightly decrease as a function of dose (when irradiated with ^{60}Co).

In literature the FWC definition can be ambiguous. In practice three types of saturation of the CCD may occur:

1. FET saturation

The linear area of the on-chip FET is not unlimited. Depending on the operating conditions, the output FET may saturate before the pixels are saturated.

2. Surface trapping

When large amounts of electrons fill the potential well some may reach the MOS surface and recombine with holes, which are very abundant here. Charge can also be spilled into neighbouring pixels, i.e. blooming.

3. Blooming

Blooming depends on the differences in the potentials of the three phases. When the difference becomes small, the limiting potential walls are lowered, and charge will spill into the neighbouring pixels. Unlike the previous case, charge is not lost in this process.

2.3.7 Gain and Noise

The noise and gain of the output FETs were investigated on EEV devices [1], but even after $3.6 \cdot 10^9 \text{ cm}^{-2}$ protons, only a slight increase in the noise was detected. ($8.2 e^- \text{ rms}$ to $8.35 e^- \text{ rms}$)

Hopkinson [6] did not detect any change in the noise on the Thomson CCDs when performing ^{60}Co irradiation, except when the reset voltage threshold exceeded the operating value at 20 kRad.

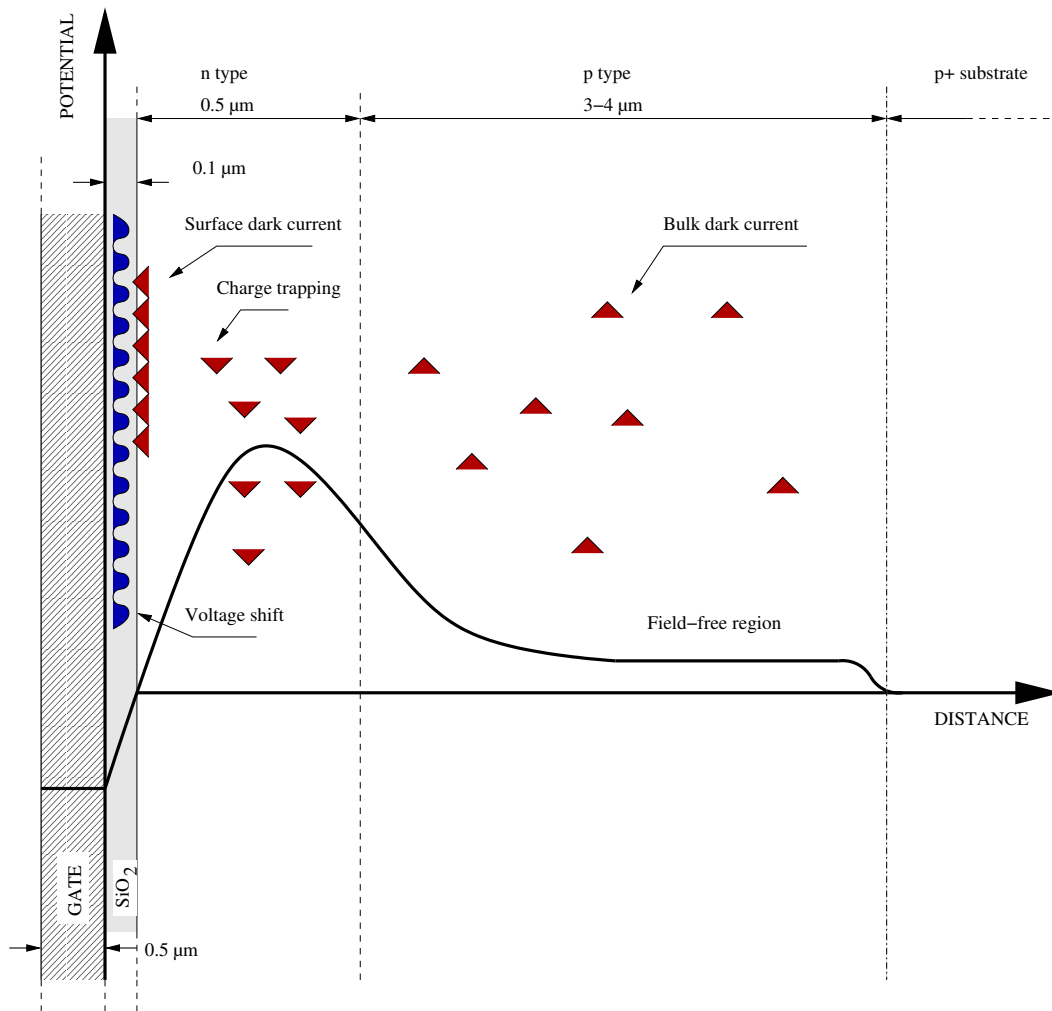


Figure 2.10 Radiation effects are here plotted into the figure 2.2. The effects illustrated here are partially created by ionizing and partially by displacement damage.

2.4 Key Parameters in a Nutshell

The table below gives a very rough overview of the parameters affected in space radiation. Here the CCD 47-20 used in the MONS telescope was kept in mind, operated in inverted mode. The expected importance of an effect is related to a specific type of radiation and marked as

“++” : very important

“+” : should be investigated

“-” : minor issue

“- -” : no problems expected

Parameter	Ionizing Damage	Displacement Damage
CTE degradation	-	++
Voltage Shift	+	-
Dark Current		
- surface*	-	--
- bulk	-	+
- spikes	-	+
- RTS	--	-
Power Consumption	-	-
Full Well Capacity	+	--
Gain and Noise	-	--

*: Surface dark current becomes significant, if the CCD goes out of inversion due to voltage shifts. Otherwise no problems are expected here.

Since the MONS CCD is cooled to cryogenic temperatures, the dark current issue may be minor.

Part II

CCD Radiation Testing

Chapter III

Experimental Work

3.1 Test Plan

Based on the theoretic and empirical results stated in the previous chapters, the CCD test plan was concentrated on the issues stated below:

- Gain and read out noise
- Full well capacity
- Charge transfer efficiency
- Dark current
- Substrate voltage shift

Two CCDs were available for testing, both Marconi CCD 47-20 backside illuminated and engineering grade, which means, that the CCD may have some serious problems, and just barely is able to output a signal. The CCD was first characterized based on a detailed test plan:

3.2 CCD Characterization

3.2.1 General Visual Inspection

The CCD was examined for structural peculiarities like hot columns, defective pixels, defects in the pixel mask and similar. Since the CCDs were of engineering grade quality, this step may reveal several problems.

Procedure: Some pictures were taken when the CCD was hot. The increased dark current reveals peculiarities as stated above.

3.2.2 Gain and Read Out Noise

Gain is the total amplification factor, describing the relationship between the collected amount of electrons in a pixel, and the actual digital number output by the ADC. Furthermore the read out noise was determined.

This was done using the photon transfer method.

Description: The photon transfer method (or variance method) uses Poisson statistics in order to estimate the gain G_{ADU} and read out noise (RON).

Let N_e and σ_e^2 be the number of electrons counted in a CCD frame and the corresponding variance. Due to the Poisson nature of the photons, and thereby the generated electrons, one may write:

$$N_e = \sigma_e^2 \quad (3.1)$$

N_{ADU} and σ_{ADU}^2 are the corresponding values expressed in digital numbers, thus:

$$N_e = G_{ADU} \cdot N_{ADU} \quad (3.2)$$

and

$$\sigma_e^2 = G_{ADU}^2 \cdot \sigma_{ADU}^2 \quad (3.3)$$

where the gain is expressed in e^-/ADU . Dividing the two equations with each other results in

$$G_{ADU} = \frac{N_{ADU}}{\sigma_{ADU}^2} \quad (3.4)$$

Thus, when plotting the noise as a function of the photon irradiance, the slope corresponds to the gain factor.

In practice there are additional noise sources such as dark current noise and RON . These can be subtracted first. Furthermore no flat field or bias exposure is entirely flat, fluctuations will contribute to σ_{ADU}^2 . This can be corrected by using two flat field exposures and two bias exposures (i.e. exposures with zero integration time) $F0, F1, B0, B1$. Those two frames are then subtracted and the variance is computed afterwards, i.e.:

$$G_{ADU} = \frac{(F0 + F1) - (B0 + B1)}{\sigma_{F0-F1}^2 - \sigma_{B0-B1}^2} \quad (3.5)$$

The computation of the read out noise is straightforward, when G is known:

$$RON = G_{ADU} \frac{\sigma_{B0-B1}}{\sqrt{2}} \quad (3.6)$$

Procedure: At any temperature two bias and two flat field exposures were made. A little script was written, which calculates the gain and noise from these frames.

3.2.3 Full Well Capacity

The full well was already defined in section 2.3.6. Note that the pixels can still hold more charge when the whole chip is irradiated with light, here the potential wells are completely filled with charge saturating the CCD.

Procedure: A green non-stabilized plain light emitting diode (LED) projected light on the CCD. 10 x 2 flat field exposures were taken at various LED

intensities. The pictures were bias subtracted with respect to gradients over the CCD determined by the over-scan area of the CCD frame. In addition a residual bias frame created from 5 median filtered bias frames were subtracted. A featureless area of the CCD was selected, and the mean value was determined. The variance was found by subtracting the two flat field exposures from each other, since the flat field exposures were not really flat. The variance of the subtracted frame was found and plotted versus the previously found mean value. The signal level, where this curve breaks, is defined as the full well capacity. This test was performed at five different temperatures for the gamma ray irradiated CCD.

3.2.4 Charge Transfer Efficiency

Charge transfer efficiency (CTE) can be divided into two types:

1. Global CTE

This is the overall mean CTE of the CCD, and can be determined by the Fe-55 method described below.

2. Local CTE

Local CTE is associated with local traps and can be discovered by the pocket pumping technique, which is described in [10]. This technique enables one to determine the position and depth of a trap. This has not been investigated further in this thesis.

Description: ^{55}Fe measurements is the most accurate way of determining the CTE. ^{55}Fe is a x-ray source emitting a strong line at 5.9 keV and a series of weaker lines. When a 5.9 keV x-ray photon hits a pixel, 1620 electrons are released in the silicon material. When reading out the CCD, some of these electrons are trapped, and this loss of charge during the transfer cycle characterizes the charge transfer efficiency.

To determine the parallel CTE, a CCD is exposed to these x-rays and the lines are stacked afterwards into a composite trace. This is illustrated in figure 3.1. The slope of the ^{55}Fe signal corresponds directly to CTE loss in the parallel registers. Thus, the CTE can be determined by the following equation:

$$CTE = 1 - \frac{S_D(e^-)}{X(e^-)N_P} \quad (3.7)$$

where S_D is the average deferred charge after N_P pixel transfers. $X(e^-)$ is the x-ray signal (i.e. 1620 e^- for an ^{55}Fe source).

Procedure: The ^{55}Fe source was simply placed in front of the CCD, and the CCD was exposed three times in 10 sec. The ^{55}Fe hits were identified with an IDL program kindly provided by Anton Norup Sørensen, IJAF. For the proton irradiation tests, this program was modified, since only half of the CCD was subjected to irradiation. The actual CTE determination happened by importing the results into a plotting program (xmgrace). The slope was determined by linear regression, and from this a CTE value was found.

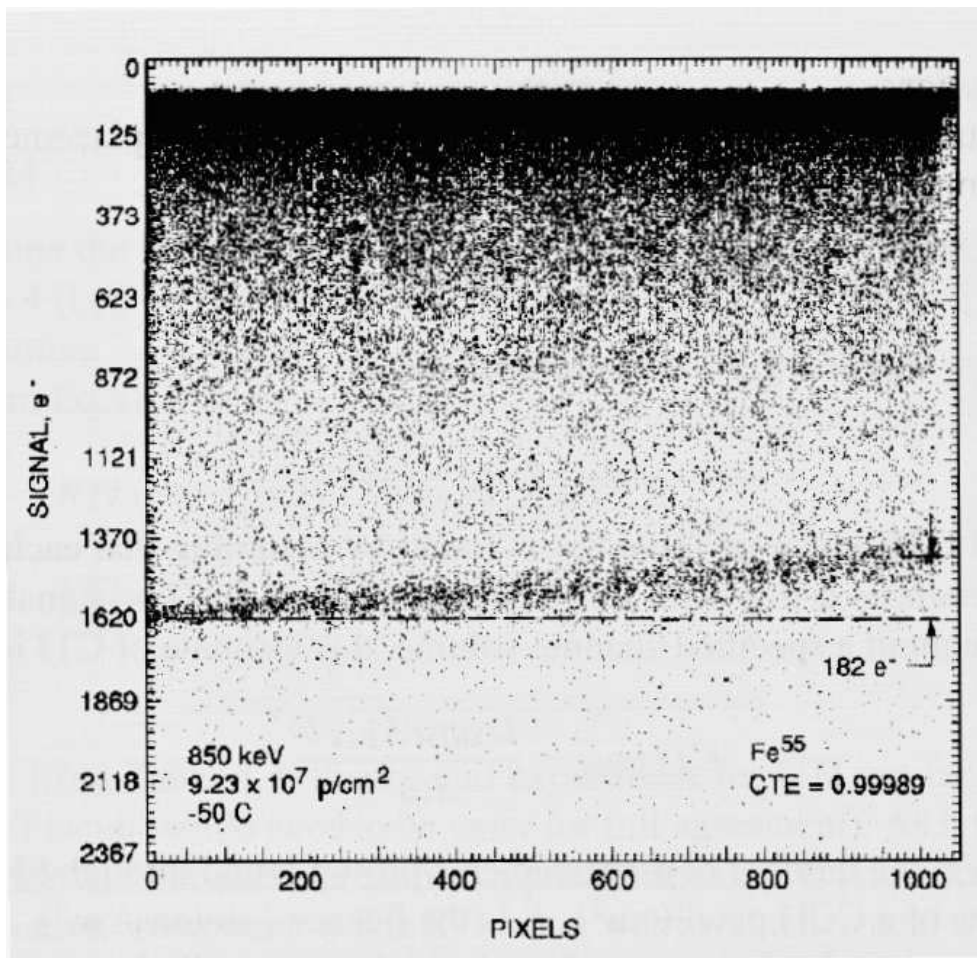


Figure 3.1 A horizontal ^{55}Fe x-ray transfer plot. *Source: [7]*

3.2.5 Dark Current

The mean dark current as a function of temperature, as well as the distribution and the amount of hot pixels were examined. Especially at the γ -ray irradiation campaign the CCD was also taken out of inversion by alternating the substrate voltage.

Mean Dark Current

Procedure: The CCD was kept totally dark for 6 different integration times, and these were adjusted to the temperature accordingly. The actual dark current value was then found by a shell script, which subtracted the over-scan bias and residual bias value. Using the gain value found previously the dark current measures were plotted versus the integration time. The slope of the curve is the dark current generation rate.

This was repeated at temperatures until $-100\text{ }^{\circ}\text{C}$. At and below this temperature the dark current was too low to be measured effectively (except for the proton irradiated device).

Dark Current Non-Uniformity

The dark current non-uniformity, or dark signal non-uniformity (DSNU), is usually defined as simply the variance of the dark current (e.g. [9]). This was only measured at the γ -ray irradiated device.

Procedure: A single dark frame was selected with a moderate amount of dark current. The signal variance of a bias subtracted frame was used for DSNU determination.

Hot Pixels

There is no final definition of when a pixel is a hot pixel. After experimenting with various definitions such as “all pixels which have $> 2\mu_{frame}$ in two frames”, the method used was simply to count the pixels above a selection of certain thresholds.

Procedure: Three frames were taken, and compared pairwise. A hot pixel had to appear in two frames to be successfully detected, thereby ruling out cosmics and other transient phenomena. The actual result is then an average of the detected pixels in the three pairwise compared frames.

If the detected amount of hot pixels is unchanged in all comparisons, it is noted as well (which indicates the insignificance of random telegraph pixels in that case).

Substrate Voltage

Procedure: The substrate voltage could be altered by adjusting a variable resistor located in the CCD controller box. This was done in steps of 0.25 Volts, and at every step, the dark current generation rate was measured by taking two frames with (very) different integration times. These frames were then subtracted from each other, and the mean value was divided by the integration time.

This test was only performed for the γ -ray irradiated CCD at room temperature and at $-80^\circ C$.

3.3 Experimental Setup

Two backside illuminated Marconi CCD 47-20 were provided by the MONS group for radiation testing:

- CCD-0:
CCD 47-20-5-331
Serial#: 8283-07-12
- CCD-1:
CCD 47-20-5-331
Serial#: 8373-10-09

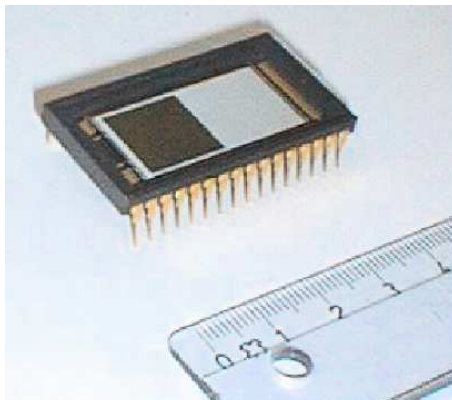


Figure 3.2 The Marconi CCD 47-20.

This CCD is a Multi Phase Pinned CCD and intended for operation in inverted mode. The active image area is 1024x1024 pixels large, or 13.3 mm x 13.3 mm, but there is also an image storage section of similar size. Furthermore some dark columns and rows are provided, which is illustrated in figure 3.3.

The CCDs were of engineering grade (“Grade 5”) quality. This is a low-cost version of the CCD, which still suits the purpose of radiation testing.

3.3.1 The CCD Camera

The CCD was mounted in a CCD camera, which previously hosted a different CCD detector. An outline of the CCD related electronics is displayed in figure 3.4. The CCD controller and the read out electronics were modified accordingly to operate the Marconi CCDs.

All operating voltages are generated by the CCD Controller; and the static ones are listed in the appendix B.1. The clocking frequencies and clocking program reside within the CCD sequencer, which had to be reprogrammed for the CCD 47-20. The sequencer was controlled by a plain PC with a special controller card inserted. A command line interface on the PC was used for sending commands to the CCD setup, e.g. when a picture was taken. The same PC was also

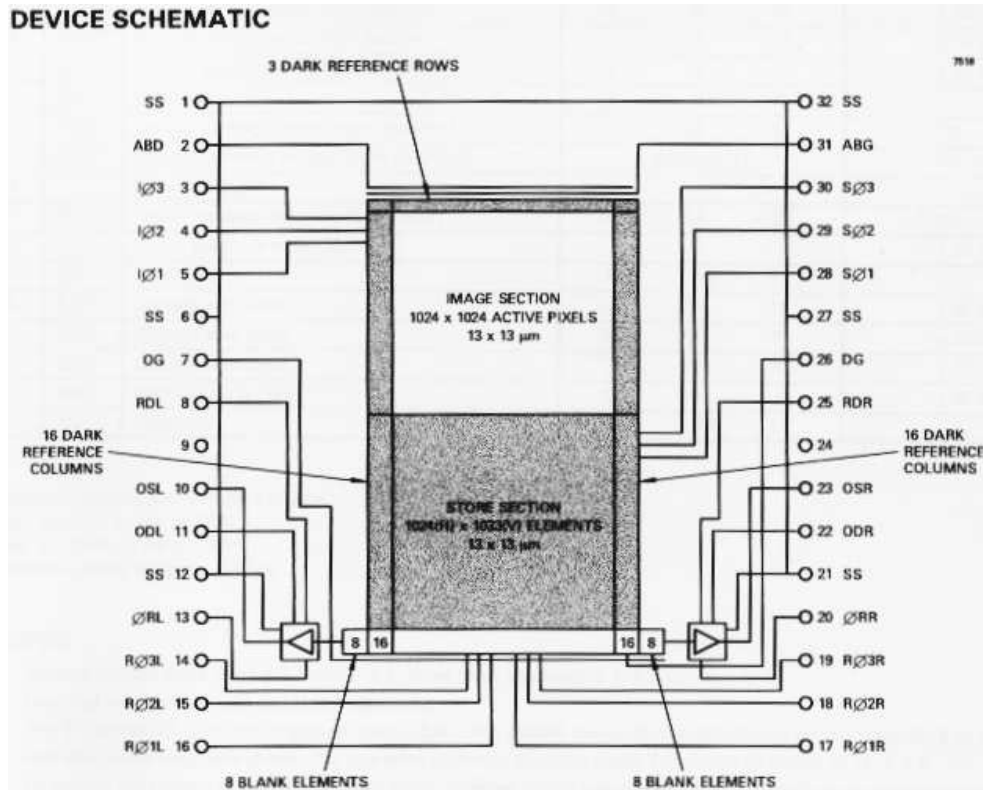


Figure 3.3 Marconi CCD 47-20 schematic. *Source: [13]*

used as a storage device, where the CCD frames were stored on a hard disk in the commonly used FITS format. From here the data could be transferred by FTP to another computer where the actual data reduction took place.

3.3.2 The Beam Line Interface

A custom beam line interface was built by the IFA workshop so the CCD camera could be mounted on one of the 5 MV accelerator beam lines. This beam line interface was built to allow in-situ determination of the above stated parameters after proton irradiation at low temperatures, and will now be described in further detail.

A blueprint of the beam line interface is displayed in figure 3.5.

Retractable LED

A plain, commercial light emitting diode could be lowered and project light onto the CCD. The diode was not stabilized in any way, but could be used for producing flat field exposures. A resistor was soldered onto one of the connectors in order to limit the current. When producing the flat fields at various intensities, a power source was regulated from 0 - 10 V. The light output of the LED is roughly proportional with the current.

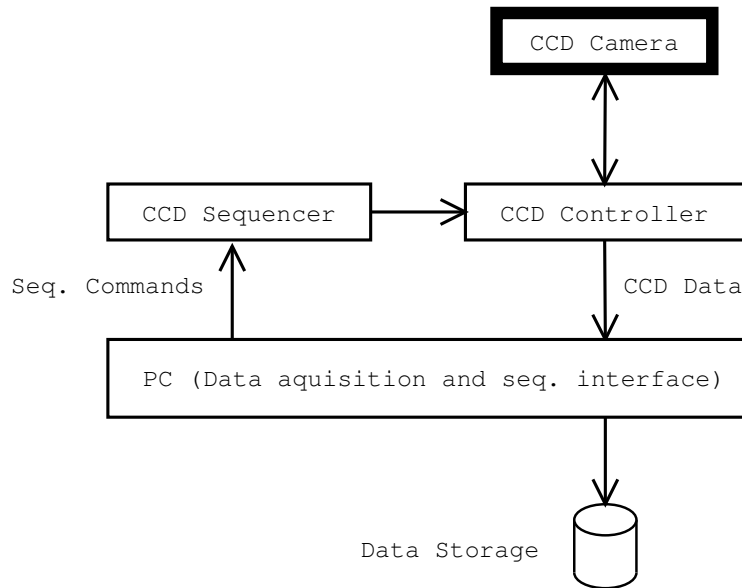


Figure 3.4 The CCD controller setup.

Retractable Beam Monitor

Here a semiconductor diode could be placed in the beam center. This diode could be turned around and on the backside some fluorescent material was glued onto, so the beam easily could be found when looking through the acryl window. Instead of a diode, an isolated metal disk could also be inserted, for a coarse current measurement.

Switching device

The switcher was a vacuum-tight device with 6 positions which could be placed on the main axis. The switch holded

- An aluminium block, 1cm thick, for stopping a proton beam and prevent light hitting the CCD.
- A Fe-55 source for CTE determination.

All other positions were empty.¹

CCD Camera Dewar

The CCD could be cooled by a dewar which could be filled with liquid nitrogen. One filling of LN2 could cool the CCD to $-120\text{ }^{\circ}\text{C}$ for two or three days. During that time it was important to maintain the vacuum in the setup, else water vapour could condensate on the CCD and may destroy the CCD.

The dewar was filled with zeolite (in the vacuum part), which acts as a getter

¹Originally a gold foil was intended for further scattering of the protons, but this idea was abandoned later on.

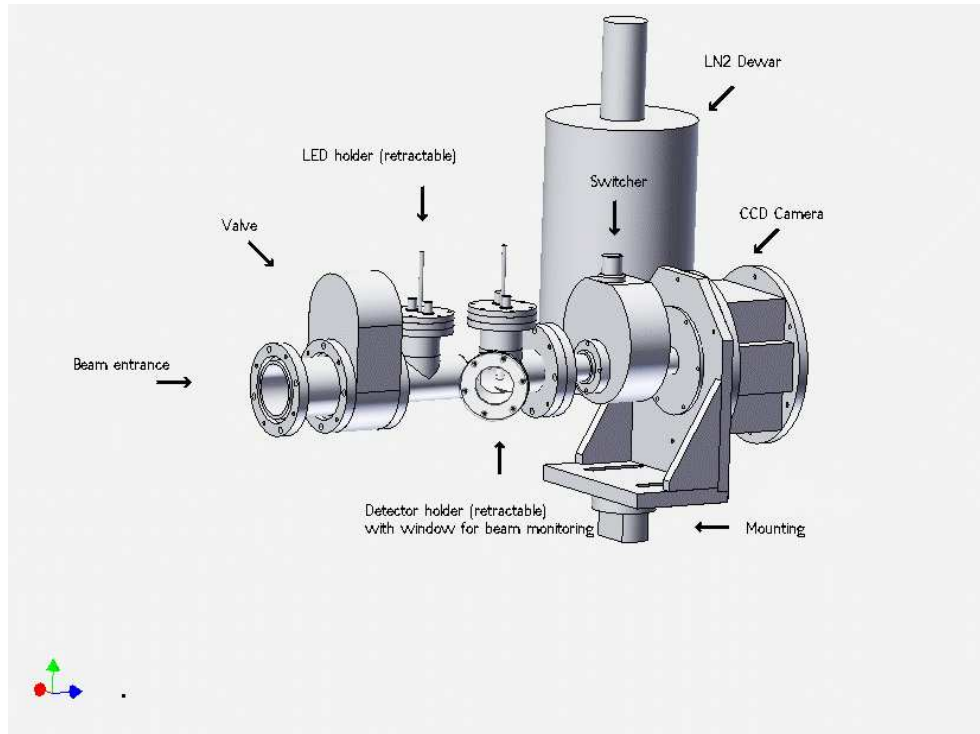


Figure 3.5 The beam line interface.

and reduces the amount of water vapour and oils within the vacuum system.

CCD Camera / Extra Beam Monitoring

The whole CCD camera could be taken off the beam line, and a visual beam monitoring device could be attached. This consisted merely of a fluorescent screen, where the exact position of the CCD in the camera housing was marked up. Thereby the position of the beam could be found.

3.3.3 Compromises

But in the end, this beam line interface was used in a slightly different way. It was decided not to use the 5 MeV accelerator for the irradiation. The reasons for this is described in the next two chapters. Instead the beam line interface was used as a mobile test bench, meaning that the performance tests could be performed right after the irradiation, which partially happened outside of IFA.



Figure 3.6 The beam-line interface, holding a light source and a Fe-55 source among other things; and the CCD camera, including read out electronics.

Chapter IV

Gamma Irradiation

4.1 Experimental Setup

Initially it was planned to perform the TID tests with bremsstrahlung from the 5 MV accelerator at IFA. But this proved unfortunately not to be too feasible a solution, since the achieved dose rates were low, and the the stability of the accelerated electron beam current was rather poor at the required dose rates. The setup at the 5 MV accelerator consisted of a water-cooled copper target, 2mm thick, where the electrons were converted to bremsstrahlung. The gamma rays passed a beam line termination made of stainless steel, which also provided a Compton equilibrium. In a distance of 1.3 meters a dosimetry film with the size of an A3 paper was placed.

The beam was very homogeneous, no significant variation in intensity was detected, but the fluence was only 1 kRad(Si)/h, at its best. This would still be acceptable, but timing problems and some major maintenance work forced me to abandon this idea. Instead the Aarhus Kommunehospital kindly provided beam-time at an accelerator which normally was used for cancer treatment.



Figure 4.1 An accelerator at the Kommunehospital Aarhus was used for the gamma ray tests. The right picture shows the entire setup, but unfortunately only the dewar is recognizable.

4.1.1 The Accelerator

The accelerator at the hospital provided a bremsstrahlung spectrum generated by 6 MeV electrons hitting a tungsten target. Beam collimators were adjusted to

match the dimensions of the CCD.

Several lead blocks were used to protect the CCD controller box where radiation sensitive CMOS components are used - the connecting cables to the CCD camera were so short that the controller box had to be placed just behind the CCD camera. The CCD was continuously read out, since the radiation effects by ionizing radiation are most prominent during biased conditions as mentioned earlier.

4.2 Dosimetry

The dosimetry was left to a employee of the Hospital. The accelerator is routinely calibrated, and the given dose is known better than 5%. Also the variation in the beam intensity across the CCD was better than 2%.

Just before the CCD, a piece of "solid water" was placed as build-up material to assure Compton equilibrium, which was necessary in order to calculate a proper dose.

The dose rate was about 0.2 kRad(Si) per min i.e. 2 Gy(Si) per min.

The hospital equipment was calibrated with respect to water, and not silicon. But by comparing the mass absorption coefficients of silicon and water, there were no significant differences in the relevant energy region.

4.3 CCD Pre-Radiation Results

4.3.1 Visual Inspection

At room temperature two defects were clearly visible on the CCD: there was a very hot spot at (x,y) 870,300 which produced a hot column across the entire CCD since the readout direction is towards lower y values¹. Furthermore there was some sort of defect in the pixel mask, which could be seen as a “switching yard”, where both signals from two columns was directed into one, leaving the other column dark. This may be one of the main reasons, why this chip was certified as engineering grade.

4.3.2 Linearity and Read Out Noise

Gain determined by the frame transfer method was plotted versus the mean signal level. This is shown in figure 4.2

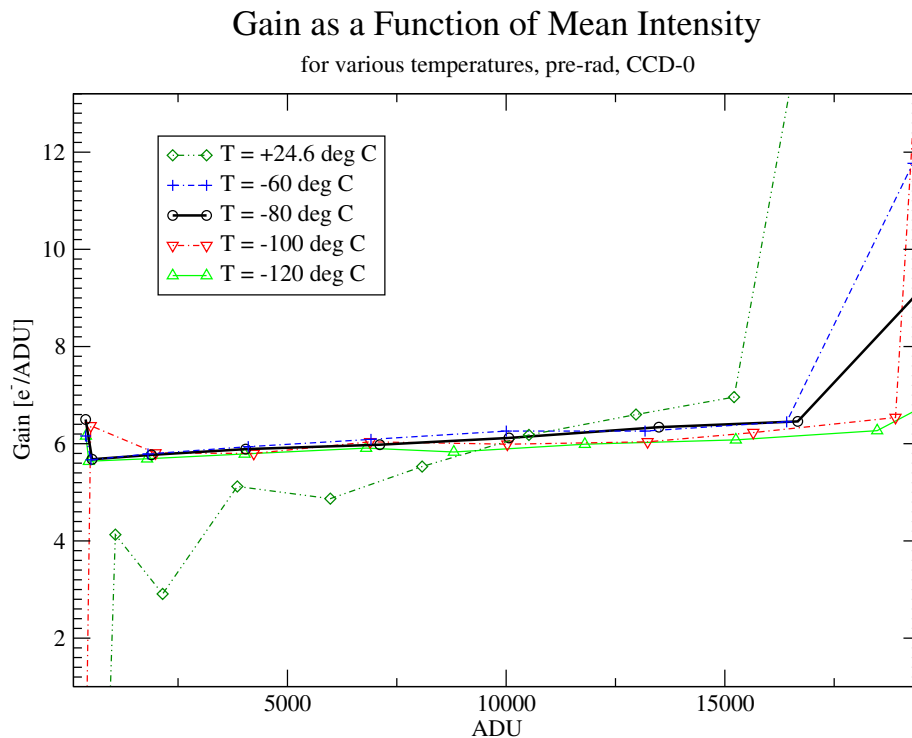


Figure 4.2 The amplifier is slightly nonlinear until 16000 ADU, thereafter saturation of the CCD FET is reached.

This figure displays several interesting features. Firstly it is seen that the CCD FET has a quite linear response between 1000 and 16000 ADU, which is

¹This implies that defects which are close to the readout register, are ruining the CCD frame more, than defects located on the edge far from the readout register.

dependent of the temperature. The FET response is more linear, the lower the temperature becomes.

Furthermore the level of saturation for the output FET is dependent on the temperature. This is a quite clear sign of that the full well capacity of the CCD was not reached, since this parameter is temperature independent according to B. Thomsen [12]. This issue has not been investigated further though. One way to do this would be to alter the clocking voltages, which definitely have an impact on the true full well capacity. If the FET saturation point is reached before the FWC is reached, alternating the clocking voltages would have no effect on the FWC.

The possibilities of alternating the operating point of the output FET is very limited, only the substrate voltage V_{SS} and the output drain V_{OD} has an impact on this feature.

The noise had a similar performance, resulting in large values, when the CCD is dominated with dark current noise, as it is, when the CCD is operated at room temperature. Figure 4.3 illustrates this. Else only a weak dependence on the signal level is observed.

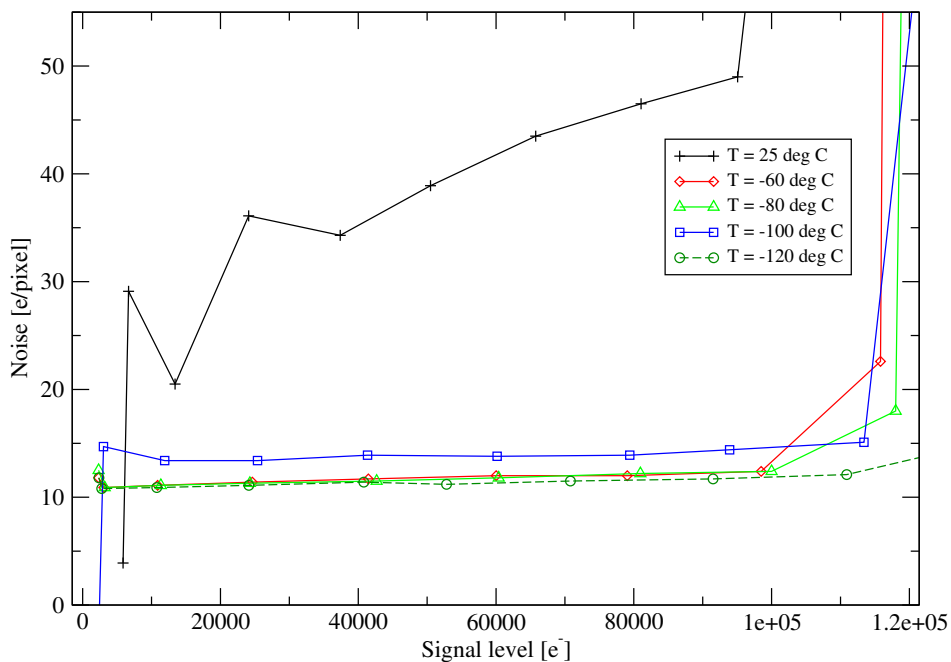


Figure 4.3 Readout noise for various temperatures for the CCD-0, prior irradiation. At room temperature, the noise is dominated by dark current noise which rises as a function of \sqrt{SIGNAL} .

4.3.3 Dark Current

Dark current is generated both at the surface and the bulk area. The temperature generation rates are different for these two dark current generation types. Marconi [9] states the following dependencies:

- Surface dark current:

$$I \propto T^3 \exp\left(\frac{-7100 \pm 100}{T}\right) \quad (4.1)$$

- Bulk dark current

$$I \propto T^2 \exp\left(\frac{-7000}{T}\right) \quad (4.2)$$

where T is the temperature (Kelvin) and I is the relative dark current. (A curve fit to the results is provided later in figure 4.8.)

The dark current have only been measured at room temperature, at -60°C and -80°C , since at lower temperatures, it may become too small to be measured effectively. When performing the data analysis, it became evident, that the CCD was not entirely dark during the exposures. It turned out that a pirani pressure sensor emitted light, detected by the CCD. Instead of a region in the center of the CCD frame, ten of the shielded columns on one of the sides were used for dark current estimation. The measured dark current was:

Temperature ($^\circ\text{C}$)	Dark current ($e^-/\text{pixel}/s$)	DSNU ($e^-/\text{pixel}/s$)
+24.6	106.6 ± 0.1	33.02
-60.3	0.0353 ± 0.0006	0.0788
-80.0	0.0237 ± 0.0006	0.0384

4.3.4 Dark Current Distribution

At -60°C and -80°C dark current histograms are shown in figure 4.4. For higher temperatures the distribution will be broader and more asymmetric. Note the little “tail” on the histogram for -60°C . At higher temperature this tail represents the hot pixels.

As stated in the Marconi report [9], the dark signal nonuniformity is often defined as the standard deviation of the dark signal generation rates of each pixel. This definition was used in this thesis. The measured results are presented in the table above.

4.3.5 Hot Pixels

The amount of hot pixels as a function of temperature is stated in the table below. Note that the calculated dark current threshold levels are only approximate. The “=” sign means that the same amount of hot pixels were detected in all three pairwise comparisons of the three frames. Elsewhere the detected amount is an approximate average. The frame size was reduced, to keep out one particular bad column, resulting in an effective area of 839520 pixels.

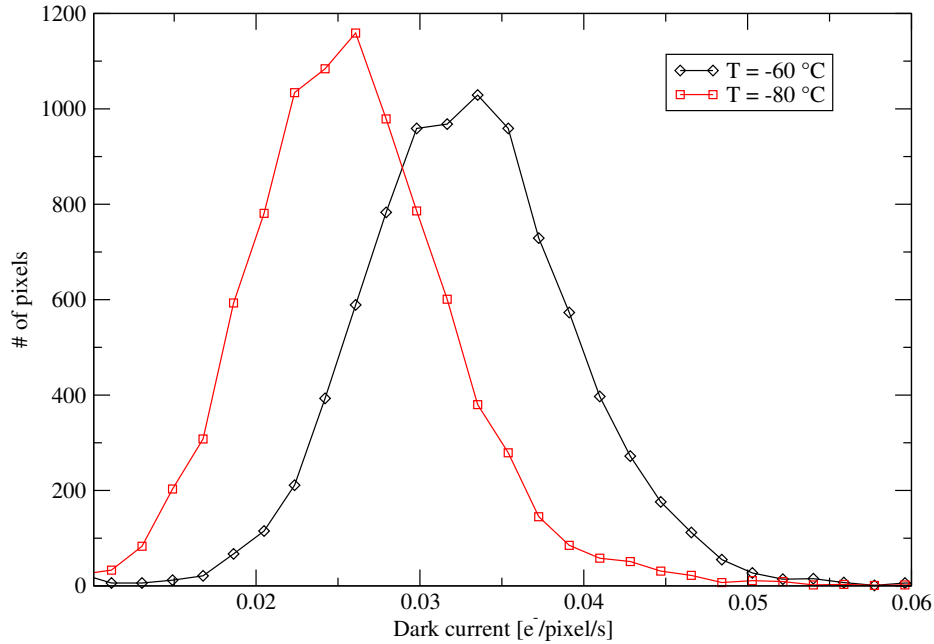


Figure 4.4 Dark current histograms at two different temperatures. The non-uniformity was $0.0788 e^-/pixel/s$ at $-60.3\text{ }^\circ\text{C}$ and $0.0384 e^-/pixel/s$ at $-80.0\text{ }^\circ\text{C}$

Temperature $^\circ\text{C}$	DC threshold ($e^-/pixel/s$)	#hot pixels detected
+25	520	2050
	310	900
-60	15	= 2
	5	50
	2.5	15
-80	15	= 0
	5	= 1
	2.5	15
-100	2.5	= 0
	1.3	= 0
-120	1.3	= 0
	0.75	= 0

At cryogenic temperature, the exposure time was 120 sec (at room temperature some exposures were made at 20 sec, and some at 120 sec). Only at lower dark current thresholds, when more hot pixels are detected, there is a variation in the number of hot pixels detected in the frame-pairs. This could originate from the presence of random telegraph signals.

4.3.6 Substrate Voltage

This important test was done at room and the base line temperature -80°C . In figure 4.5 only the latter test result is provided.

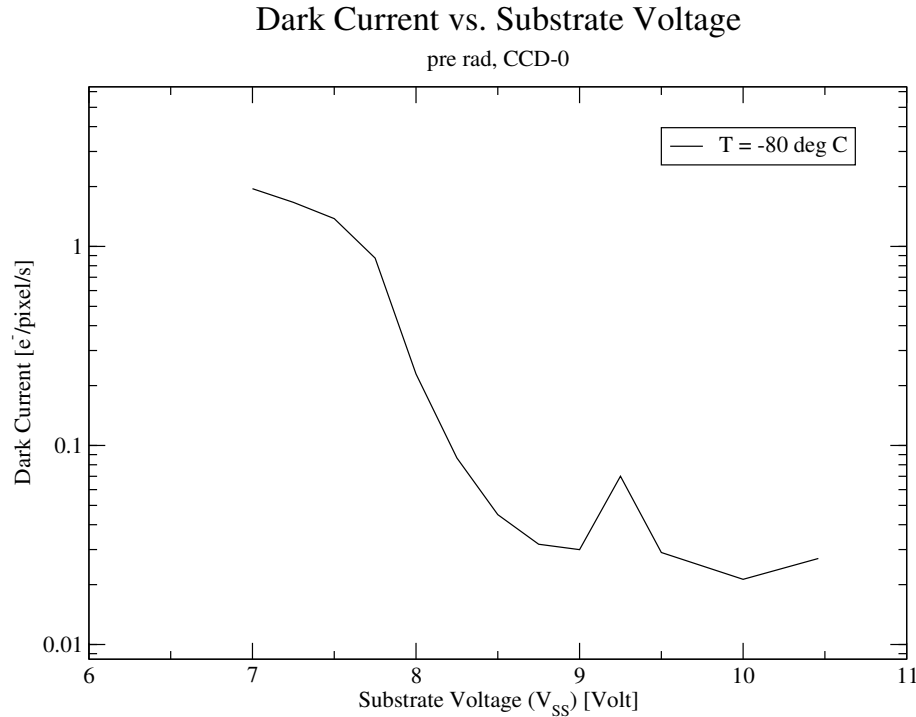


Figure 4.5 Dark Current Rate rises quickly, as the CCD is taking out of inversion.

As the CCD is taken out of inversion, dark current generated at the MOS interface region begins to dominate, as expected. As illustrated later, this will happen earlier, after the CCD has been subjected to ionizing radiation. The little peak at 9.25 Volts is considered as an outlier, and is not a real feature (see also figure 4.11, where the results are plotted again in a linear scale).

4.3.7 Full Well Capacity

The actual full well capacity, where charge is blooming from one pixel into the next, could not be determined, since the output amplifier reached saturation before. However, this happens at 100.000 e⁻, which is the same number stated in the Marconi CCD 47-20 product specifications. This leads to the thought, that the true full well capacity never can be achieved due to the setting of the operating point of the on-chip FET. Figure 4.6 illustrates this.

4.3.8 Charge Transfer Efficiency

Both serial and parallel CTE was determined at various temperatures, the results are presented in the table below:

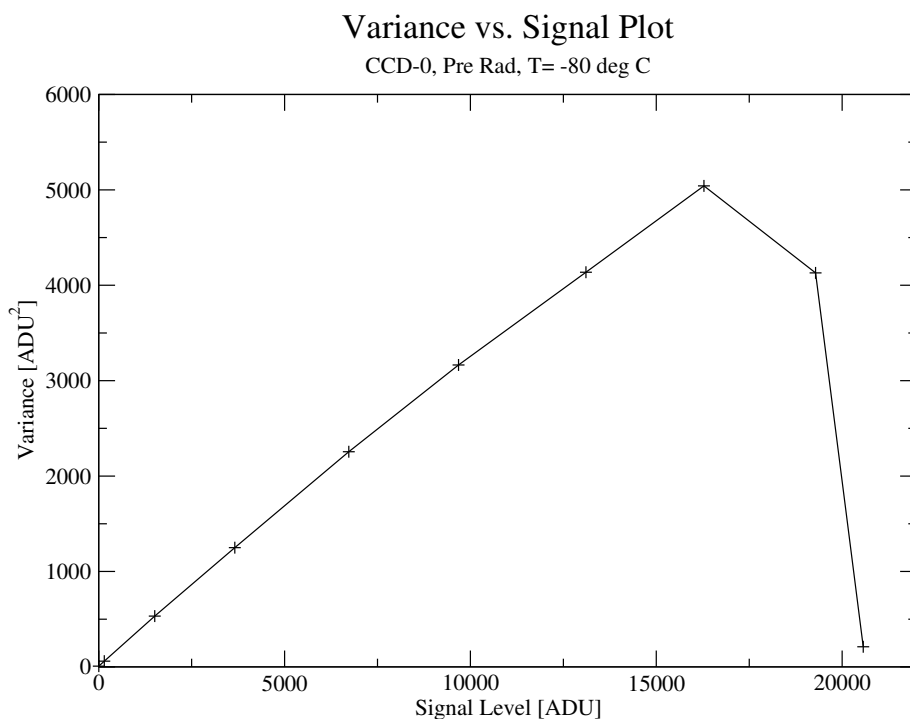


Figure 4.6 The on-chip output amplifier saturates at approximately $100,000 e^-$.

Temperature °C	Parallel CTE
+24.6	> 0.999993 ± 0.000003
-60.1	0.999999 ± 0.000001
-80.0	0.999999 ± 0.000001
-99.7	> 0.999999 NIL
-119.5	> 0.999999 NIL

As expected, the CTE performance of the CCD is good. At -100°C and -120°C it was better than it could be measured. The CTE at room temperature is very likely to be biased by the high dark current background, since the Fe-55 exposures were in the order of 10 seconds.

Only about 10 % of the pixels were single event pixels, meaning all electrons released by the ^{55}Fe photons were confined in one single pixel. Most of the ^{55}Fe photons are absorbed in the field-free region illustrated in the figure 2.2. Electrons released here are not confined by a potential well and can wander to neighbouring pixels. For larger field-free regions, less photons are likely to be confined to one pixel.

4.4 Total Dose Results

It was decided to irradiate the CCD-0 in three steps, 7.5 Gy, 15 Gy and 35 Gy. In all cases the entire CCD was irradiated with a bremsstrahlung spectrum, more homogeneous than 2 %, spatially.

A quick performance check of the CCD was done at ambient temperature just immediately before testing, to detect eventual changes, and after each irradiation step, the CCD was allowed to re-constitute for approximately 15 minutes, to eliminate any short term effects.

- At 7.5 Gy a quick test was done, where bias frames, dark frames, flat fields and Fe-55 exposures were taken.
- At 15 Gy this test program was repeated, but including the substrate voltage test.
- At 35 Gy only a very quick test was performed, only including bias frames, dark frames and Fe-55 exposures.
- Later a full characterization was done at all temperatures. The results from this test are used in this thesis. The other tests served more as a “safeguard”, in the case of a CCD failure after the 35 Gy irradiation.

4.4.1 Visual Inspection

No visible degeneration was observed, except for an increase in dark current at room temperature.

4.4.2 Linearity

There was not expected any significant change in the gain response, but the gamma irradiation seems to have decreased the amplification a bit. The Fe-55 CTE determination technique also gives an estimate of the gain, since the amount of electrons generated by a Fe-55 photon is known. According to this, the temperature dependence of the gain factor has also increased, but this is less relevant to MONS, since the CCD detector is operated at a fixed temperature. The results are stated in the table below, and indicates a decreased sensitivity after irradiation.

Temperature ($^{\circ}C$)	Gain (e^{-}/ADU) Pre Rad	Gain (e^{-}/ADU) 35 Gy
+25	6.25	~6.6
-60	5.96	6.37
-80	5.96	6.23
-100	5.96	6.08
-120	5.96	5.93

The figure 4.7 shows the relative response of the output amplifier towards various signal levels, determined by the frame transfer method, before and after irradiation with γ -rays at -80°C . No significant change in the linear behaviour is detected; the performance is still within $\pm 6\%$ but it can be seen that the maximum output signal is decreased, what will be investigated further later on.

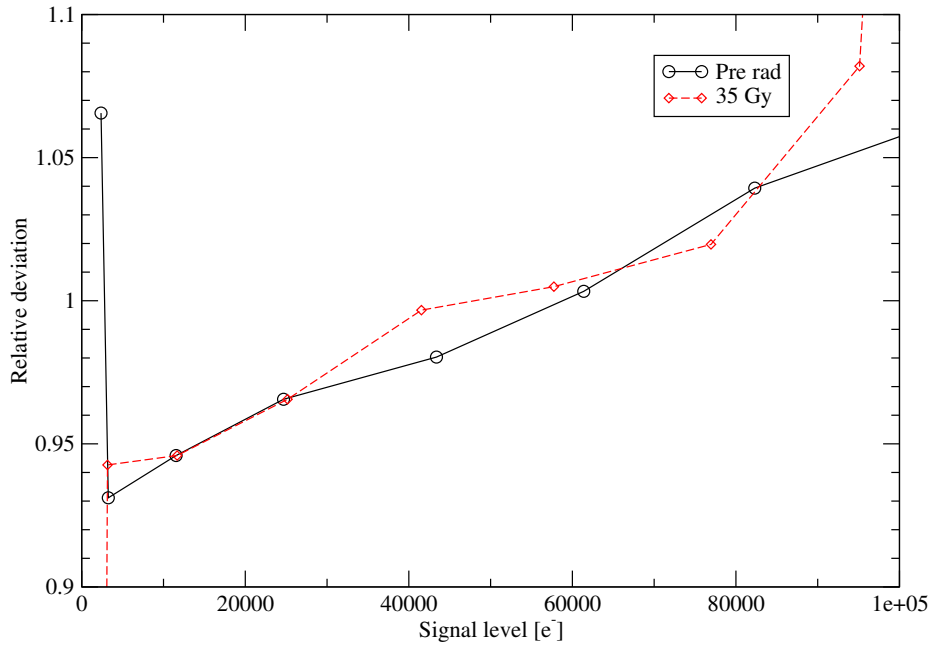


Figure 4.7 CCD linearity at -80°C remains quite unchanged after CCD irradiation.

4.4.3 Dark Current

The measured dark current was:

Temperature ($^{\circ}\text{C}$)	Dark current ($e^{-}/\text{pixel}/\text{s}$)	DSNU ($e^{-}/\text{pixel}/\text{s}$)
+25.9	112.6 ± 0.1	81.4
-60.2	0.068 ± 0.003	0.147
-80.1	0.0273 ± 0.0006	0.050

Dark current has increased slightly after irradiation, but at -80°C no significant increase is observed. Figure 4.8 illustrates the increase and curve fits to the bulk dark current equation 4.2. The “semi-theoretical” curve fit, is from the Marconi dark current equation 4.2, where the “energy level term” is kept fixed to -7000 , as it is in the bulk dark current equation. However, both the surface dark current equation (not shown in figure) as well as the bulk dark current equation can be fitted to the pre rad results, mainly due to the lack of data points. On the other hand, most of the dark current must arise from bulk defects, since the

CCD is still inverted (which is visible in the substrate voltage test), also after the irradiation with gamma rays.

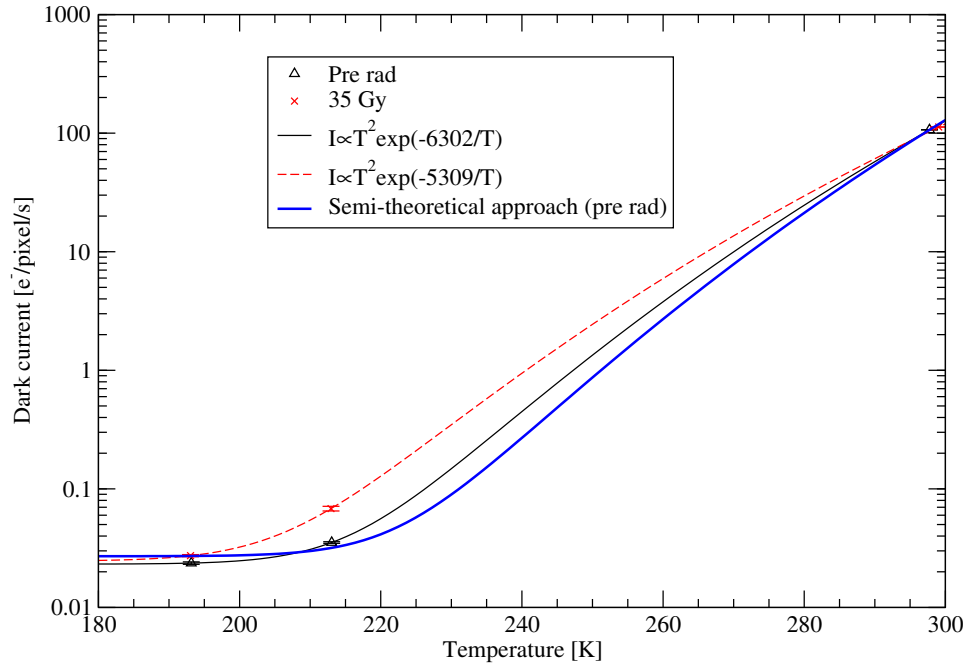


Figure 4.8 Dark current values at room temperature, at -60°C and -80°C , measured on the CCD-0 prior and after irradiation.

4.4.4 Dark Current Distribution

The dark current distribution, as shown in figure 4.9, has changed a little at the baseline temperature. The results are mentioned in the table above. The tail of the histogram for the higher dark current values, are the hot pixels.

4.4.5 Hot Pixels

Compared with the results stated in section 4.3.5, the amount of hot pixels have increased slightly, mostly since the overall dark current has risen.

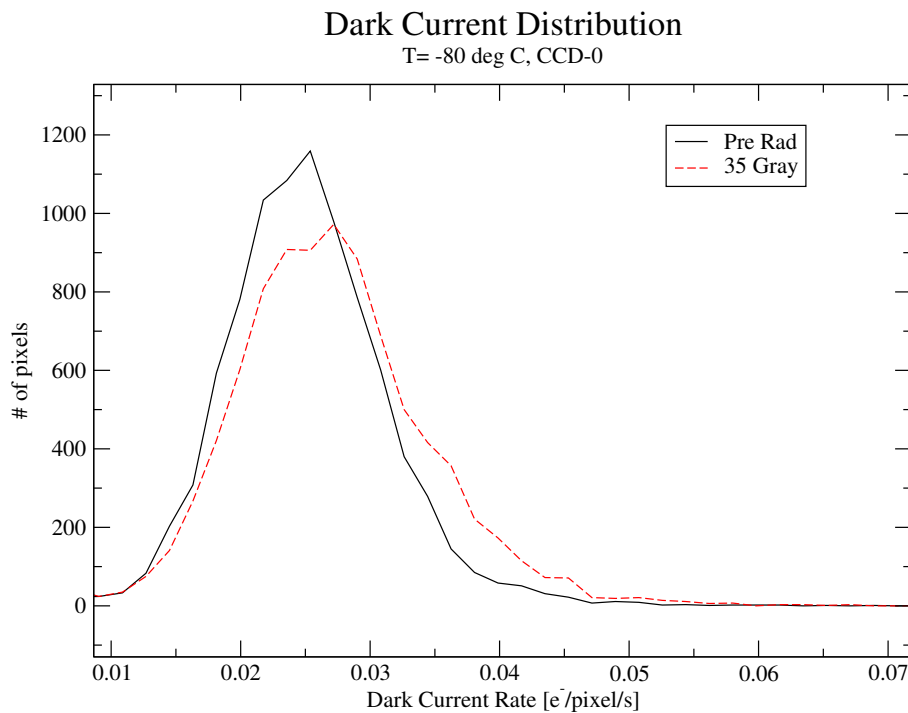


Figure 4.9 Dark current histograms before and after gamma ray irradiation. Dark current is still barely detectable.

Temperature $^{\circ}C$	DC threshold ($e^{-}/pixel/s$)	#hot pixels detected
+25	1980	130
	990	770
-60	16	= 9
	5.3	60
-80	15.6	= 0
	5.2	= 2
	2.6	= 10
	1.3	85
-100	2.5	= 0
	1.3	= 2
-120	2.5	= 1
	1.2	= 1
	0.74	= 1

4.4.6 Substrate Voltage

A flat-band voltage shift was clearly observed. The figures in fig. 4.10 and 4.11 clearly show the effect of the ionizing radiation. At $-80^{\circ}C$ the voltage shift was approximately 0.1 ± 0.02 V/kRad(Si).

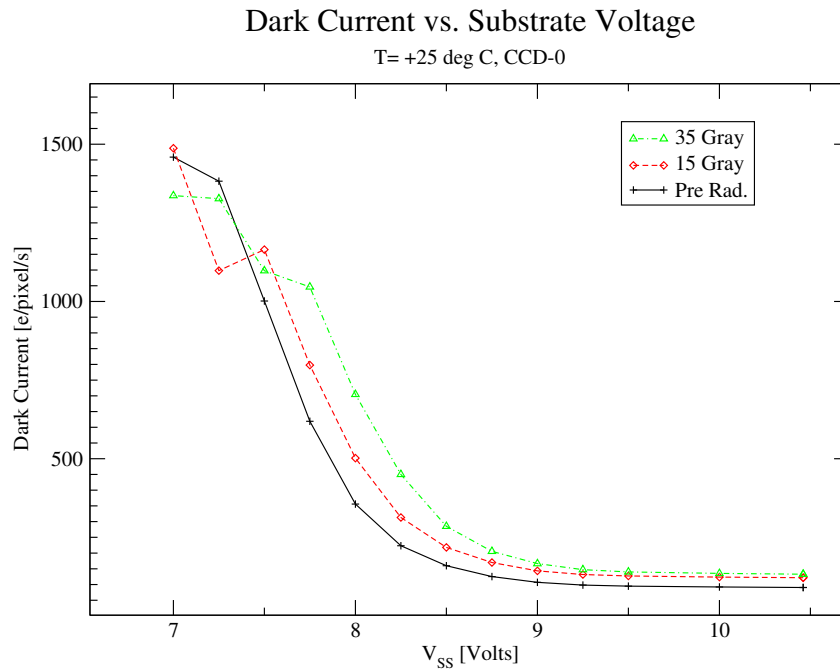


Figure 4.10 Voltage shift at room temperature at various irradiation levels.

4.4.7 Full Well Capacity

The saturation of the output amplifier was reached at approximately $100,000 e^-$, and this value was slightly decreasing as for higher doses of ionizing radiation. After 35 Gy(Si), the signs of saturation were achieved at $80,000 e^-$. The figures 4.12 and 4.13 illustrate this. Note that a little change in figure 4.12 can be seen, indicating a change in the gain.

4.4.8 Charge Transfer Efficiency

Again, parallel CTE was determined at various temperatures, the results are presented in the table below:

Temperature °C	Parallel CTE	
+25.9	NIL	NIL
-60.2	0.999995	± 0.000003
-80.1	0.999985	± 0.000002
-99.8	0.999978	± 0.000002
-119.6	0.999983	± 0.000002

CTE has degraded significantly, which is surprising, since CTE is not associated with ionizing damage. There are two possible explanation for this:

1. There was a significant hadron (neutrons, protons ...) flux present, or

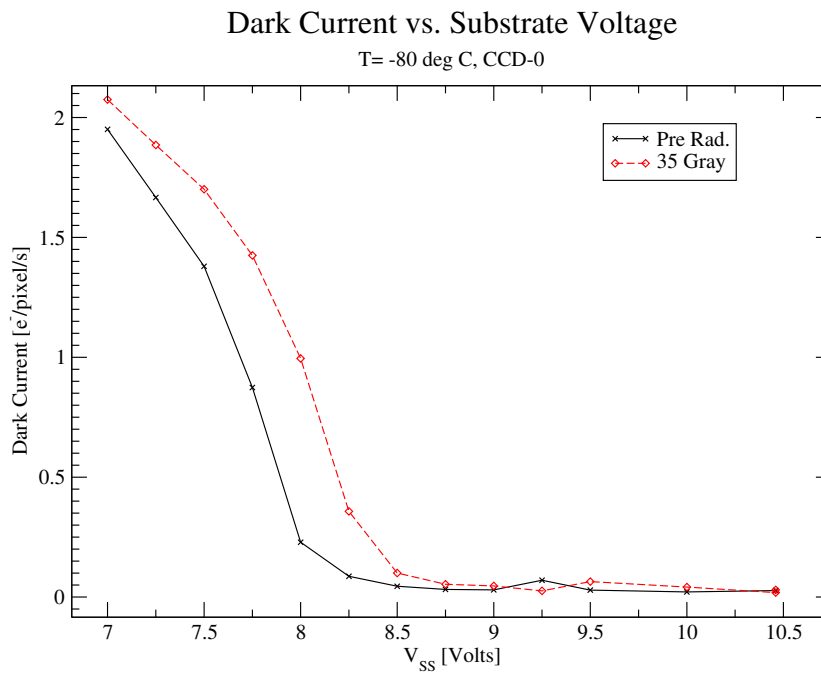


Figure 4.11 The voltage shift is evident and by reading from the graph, it is estimated to be approximately 0.1 ± 0.02 V/kRad(Si).

2. The gamma rays were too energetic, resulting in a significant amount of displacement damage.

The personel from the hospital assured that there is no detectable hadron flux present at that energy (bremsstrahlung from 6 MeV electrons), and thereby ruling out 1). Nonetheless, the conclusion has to be, that this extra degeneration is not seen in space, since a) the bremsstrahlung spectrum is more soft in space, since the electrons typically have lower energies, and b) The major source - and that is a fact - of displacement damage encountered in space, is caused by the trapped protons.

CTE measurements at room temperature were impossible due to the high dark current.

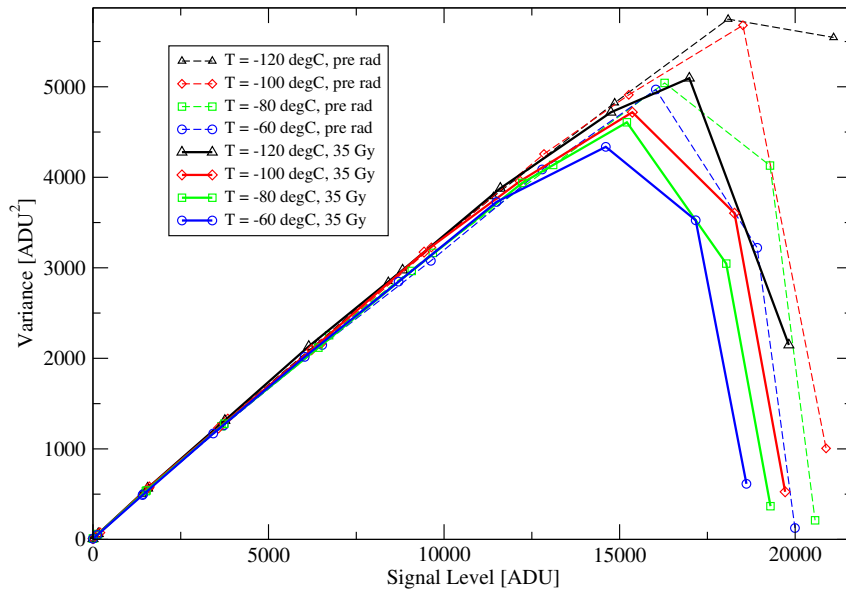


Figure 4.12 At all temperatures, a decrease of the maximum signal capacity of the detector can be seen.

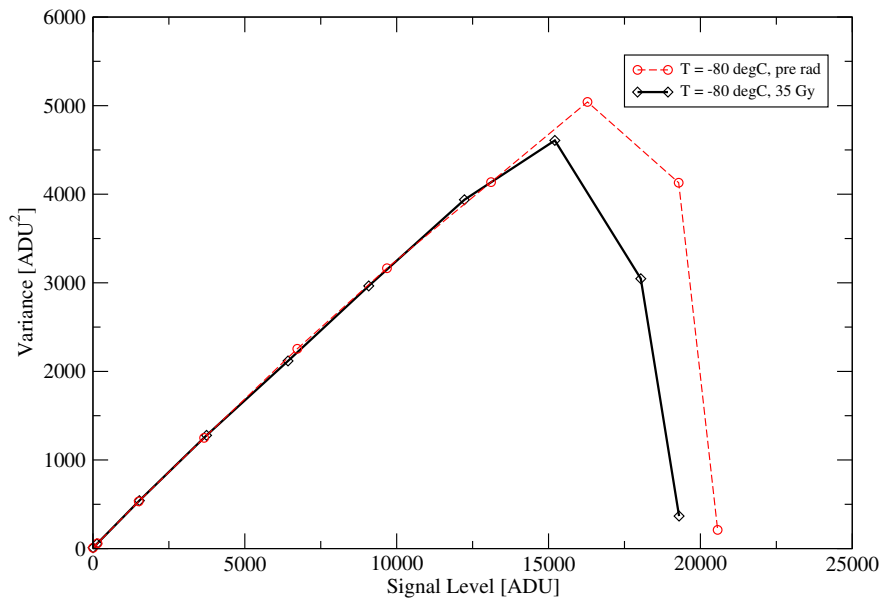


Figure 4.13 The same figure as 4.12, showing only the results at -80°C .

Chapter V

Proton Irradiation

5.1 Experimental Setup

The planned irradiation with 2 MeV protons had some serious limitations. First of all, the energy was so low that the Bragg peak of the protons may lie within the depletion layer. Since the exact architecture of the CCD is unknown, this would mean a large uncertainty on the actual applied dose on the CCD. In fact, any gradients in the deposition of energy within the CCD may be highly undesirable in this case.

Furthermore, the dosimetry was complicated by the fact that the fluence estimation at low currents is almost impossible by the existing facilities at the beam-line. The CCD should receive a total fluence of 10 MeV protons in the order of $5 \cdot 10^9 \text{ protons/cm}^2$. One 2 MeV proton makes as much displacement damage per unit length as 4.64 10 MeV protons (see appendix B.3). A fluence of $1.08 \cdot 10^9 \text{ protons/cm}^2$ which corresponds to a total charge of $1.73 \cdot 10^{-10} \text{ Coulomb}$. Integrated over 10 seconds, this equals a current of only 1.73 nA, which is bearably measurable with a common Faraday cup.

For this reason, the particle-detecting diode was built into the setup, but the next problem was to aim the only about 1 cm^2 large proton beam at the CCD. This may result in a very time consuming process, perhaps even resulting in some redesign of the setup.

There was a slot of available beam-time at the storage ring ASTRID at ISA. This could be configured to provide 10-15 MeV protons quite easily, and then the decision was made to abandon the original idea of irradiating the CCD with the 5MV Van de Graaf accelerator.

Some disadvantages at the ASTRID synchrotron was identified as well: first of all, there was no chance of designing a new interface piece to the storage ring vacuum system. Also some of the wiring in the CCD camera housing can not be used in a ultra high vacuum system. Instead an “open” setup was considered. The disadvantage of this setup was, that the CCD could not be cooled during the irradiation. The CCD fixture was taken out of the CCD housing, and placed on the center of the beam line at a calibrated area. The setup is shown in the picture 5.1.

The proton beam was pulsed, providing approximately 1 or $2 \cdot 10^6 \text{ protons/cm}^2$ for each acceleration cycle every 26th second. The proton storage energy was 15.5 MeV, and the proton energy in the target was calculated to be in the order

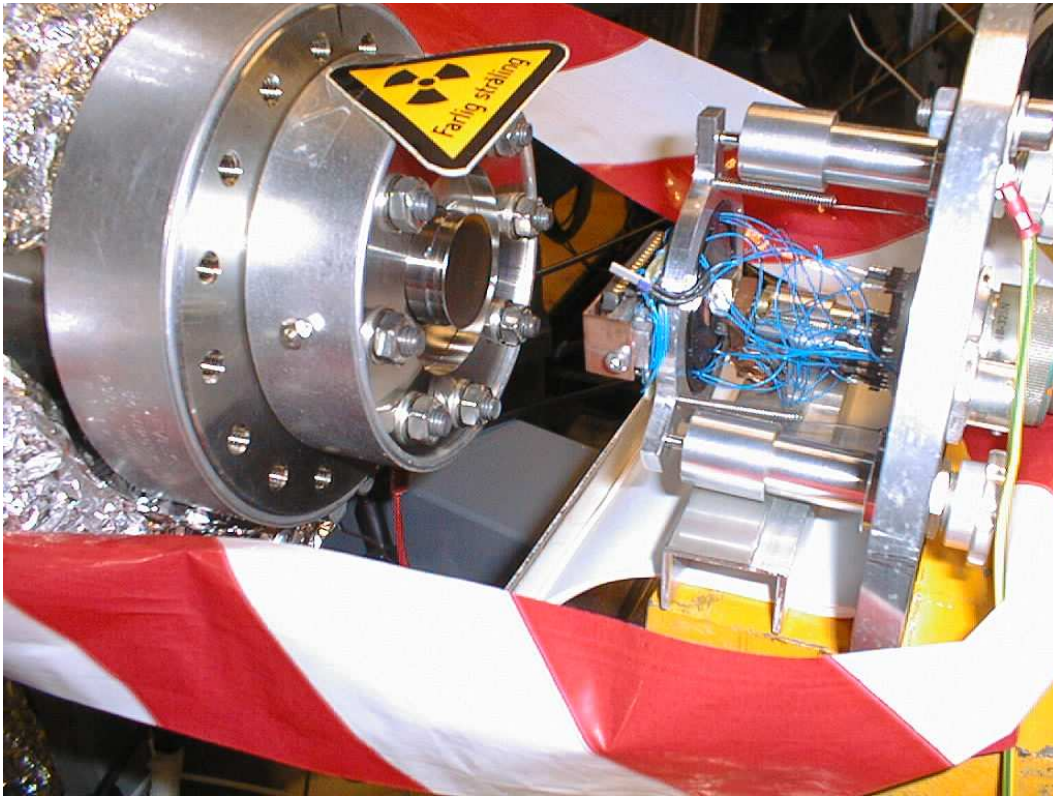


Figure 5.1 The proton irradiation setup, showing the beam exit and a glimpse of the CCD.

of 11.5 MeV. The current in the storage ring was measured all the time, and calibrated to a scintillation detector before the irradiation took place. This configuration was used to irradiate some filter samples for the MONS project during the week, and this also provided a way to monitor the stability of the beam. The beam was remarkably stable: in the entire week, the drift was better than $\pm 5\%$ in spite of various temporary failures such as a faulty quadrupole magnet and duoplasmatron ion source.

The net flux of this accelerator was extremely low. To irradiate the chip, over 2000 cycles were required, resulting in an irradiation time of 16 hours.

Problems however were encountered during the irradiation process. The irradiation started on a Saturday evening 18:30 local time, and was left for the night. Very unfortunately, the application software, which logged the monitored beam current in the ring, crashed quite early. This happened Sunday morning at 1:22. The irradiation though continued, and this would not be a major problem, since the beam performance has been very stable until then. Furthermore the quadrupole magnet failed again resulting in a sudden beam loss. By investigating the log files of the cooling water for this quadrupole magnet, it could be reconstructed that this had happened at 4:30 in the morning. At 12:30 the ion source also failed.

(I could not reach the operator in charge that Sunday evening, but the ISA people kindly provided me with an extra day of operation, so I could complete the irradiation.) The question was, how much fluence, had the CCD received by then?

The beam current monitoring program recorded approximately 700 cycles before the application crashed. During these 700 cycles, the program had integrated a current corresponding to a fluence of $1.36 \cdot 10^9 \text{ protons/cm}^2$, thus $1.9 \cdot 10^6 \text{ protons/cm}^2/\text{cycle}$, which is typical compared to the irradiation campaign which were made earlier that week. Furthermore the rate of the cycles is 125.6 cycles per hour. When the quadrupole magnet failed, at 4:30 in the morning, the irradiation was in progress for 10 hours or 1256 cycles. This corresponds then to a total fluence of $2.46 \cdot 10^9 \text{ protons/cm}^2$.

The next day the irradiation continued, but late in the evening, the ion source failed again. All efforts to re-ignite the duoplasmatron were unsuccessful, probably since it was out of gas. At that time the CCD had received an addition fluence of $1.74 \cdot 10^9 \text{ protons/cm}^2$, yielding a total dose of only $4.2 \cdot 10^9 \text{ protons/cm}^2$ at 11.5 MeV. This corresponds to about $3.85 \cdot 10^9 \text{ protons/cm}^2$ of 10 MeV equivalent protons, which is 23% less than the dose the MONS CCD will receive!

There was no chance of getting additional beam time at the accelerator, so the CCD has not been irradiated any further.

The beam size was smaller than expected, which is shown in figure 5.2. Therefore all results are average over the entire frame, which is approximately 1 cm long, and a bit less than 0.5 cm wide. The beam was calibrated in a circular region 1 cm in diameter centered on the beam axis.

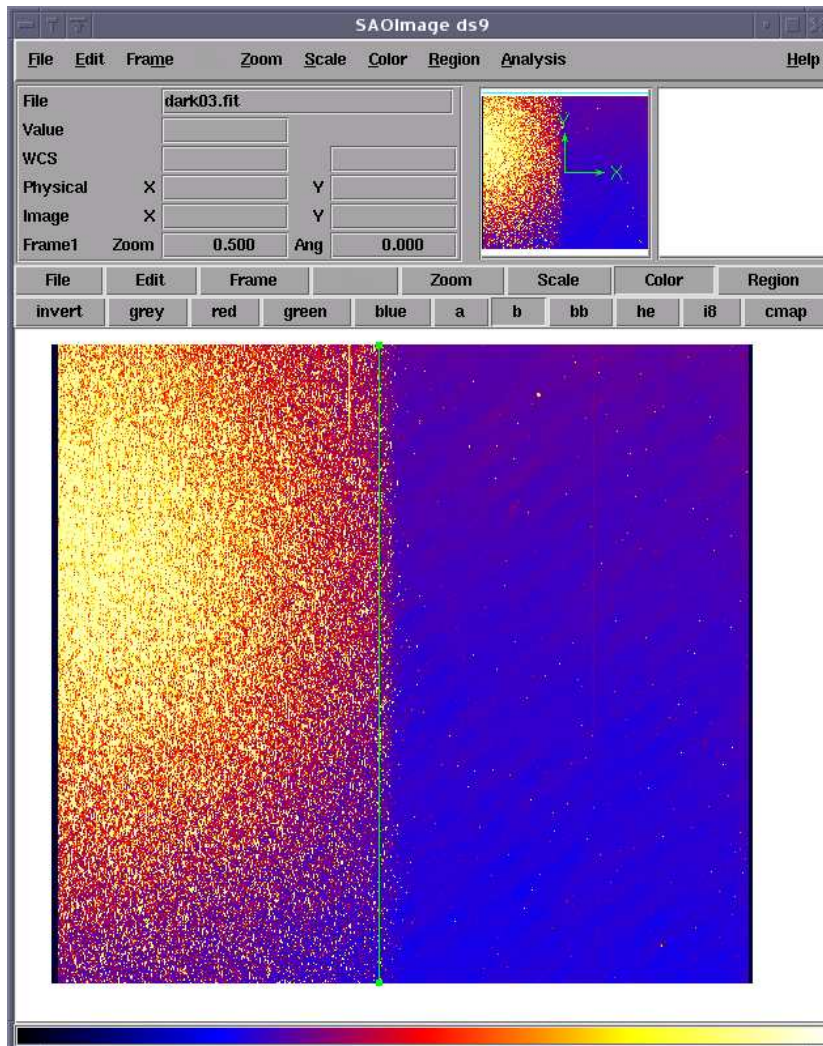


Figure 5.2 Dark current picture of the proton irradiated CCD-1. The green line marks the area which was used for post-radiation qualification.

5.2 CCD Pre-Radiation Results

The CCD-1 was chosen for the proton irradiation. This CCD had significant problems with the on-chip amplifiers. Tests with ^{55}Fe showed, that the amplification factor was about 7 times lower than it should be on both amplifiers. Instead of having a gain of about $6 e^-/ADU$, it was measured to be about $40 e^-/ADU$. This was the case on both output amplifiers. Presumably this is related to the output gate bias, pin 7 in the figure 3.3, since this is the only voltage, which is shared by both FETs, which else are physically separated from each other. Changing the voltage of this pin did not result in any improvement though. It was never figured out, what really was wrong with this chip.

The poor amplification was compensated by increasing the amplification of the external pre-amplifier.

5.2.1 Visual Inspection

The CCD showed very anomalous behaviour if exposed to moderate levels of light. It looked as if the reset FET ceased to reset when reaching a certain signal level. This resulted in unusable frames. The Fe-55 signal, though, was still far from the level where this happened, so the CCD could still be used for CTE tests. But CTE measurements were also complicated due to the poor signal to noise ratio, caused by the large read-out noise by the on-chip FET.

On the other hand visually inspecting the CCD showed very few defects. At room temperature only one large hot pixel causing a column could be seen as well as five minor columns. At -80°C only one weak hot column could be seen, and the defect causing this was located far away from the amplifier, thus only affecting the upper part of the frame. In fact, at cryogenic temperature, the CCD dark frames were very featureless.

5.2.2 Gain and Read Out Noise

Since the CCD-1 showed abnormal FET performance, the linearity test was skipped, instead gain was estimated by the frame transfer and Fe-55 technique. The results at -80°C were:

Technique	Signal level	Gain (e^-/ADU)	RON
Frame transfer	$\sim 22000 e^-$	8.50	55.2
Fe-55	$1620 e^-$	8.3	53.9

Since the output amplifier was not subjected to irradiation, this was not re-characterized after the irradiation campaign.

5.2.3 Dark Current

The dark current was measured using 800×800 frames. (This time, the pirani pressure sensor was removed during the measurements.)

Temperature ($^{\circ}C$)	Dark current ($e^{-}/pixel/s$)	DSNU ($e^{-}/pixel/s$)
+25.9	178.5 ± 0.621	51.31
-80.1	0.018 ± 0.001	0.1545

5.2.4 Dark Current Distribution

Dark current distribution differed very much from what was measured on the CCD-0. In this case, the frame was much larger than the frame used on the CCD-0, which may lead to a different variance. The high FET noise level was also biasing these results.

5.2.5 Hot Pixels

Hot pixels have also only been investigated at $+25^{\circ}C$ and $-80^{\circ}C$. Only about half of the CCD was investigated here (since only half of the CCD would be irradiated), effectively 420480 pixels.

Temperature $^{\circ}C$	DC threshold ($e^{-}/pixel/s$)	#hot pixels detected
+25	740	130
	593	770
	445	1000
-80	70	= 0
	7	= 1
	3.5	3
	1.4	45

5.2.6 Charge Transfer Efficiency

Again, parallel CTE was determined at various temperatures, the results are presented in the table below:

Temperature $^{\circ}C$	Parallel CTE
+25.9	0.999987 ± 0.000006
-80.1	0.999994 ± 0.000004

Compared to the pre-radiation results of the CCD-0 the standard error is significantly larger, due to the increased FET noise. However, the CTE is still 1σ within the results of the CCD-0.

5.3 Proton Irradiation Results

5.3.1 Visual Inspection

A very clear increase in dark current and the amount of hot pixels could be observed at both room temperature as well as cryogenic temperatures. The amount of defects were unchanged, as expected.

5.3.2 Dark Current

The dark current was measured using an area of 450 x 930 pixels of the irradiated region. In the measurements performed at room temperature the CCD was quickly saturated with dark current. Only three frames were used at this distinct temperature.

Temperature ($^{\circ}C$)	Dark current ($e^{-}/pixel/s$)	
+24.3	1025	± 58
-60.3	1.03	± 0.01
-80.1	0.354	± 0.003
-99.8	0.072	± 0.001
-119.5	0.016	± 0.001

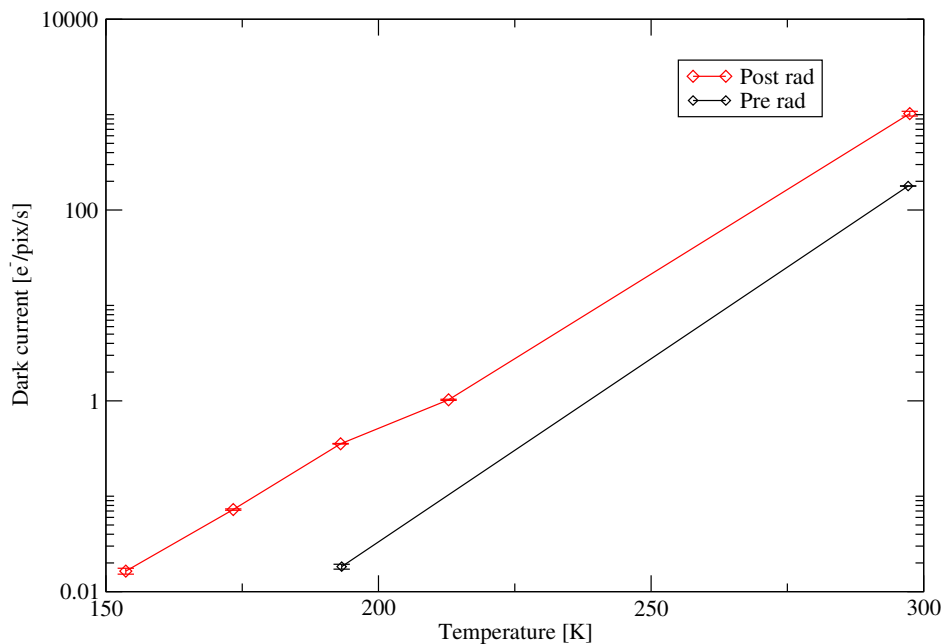


Figure 5.3 Dark current before and after proton irradiation.

5.3.3 Dark Current Distribution

Dark current distribution was not determined post rad, this would be meaningless since the proton irradiation was very inhomogeneous.

5.3.4 Hot Pixels

As shown in the table below the amount of hot pixels has increased much at room temperature compared with the pre-radiation results. As the CCD was cooled down, the amount of hot pixels was quickly reduced.

Temperature °C	DC threshold ($e^-/pixel/s$)	#hot pixels detected
+25	4450	10550
	3560	51950
	2670	73200
-60	70	204
	35	745
	7	15000
-80	70	= 34
	7	1900
	3.5	7200
-100	70	= 4
	7	220
	3.5	520
-120	70	= 1
	7	25
	3.5	53
	1.8	135

5.3.5 Charge Transfer Efficiency

The CTE post irradiation was surprisingly good, even though the error bars are large due to the poor signal to noise ratio. The results are presented in the table below:

Temperature °C	Parallel CTE
+24.3	NIL
-60.3	0.999991 ± 0.000005
-80.1	0.999988 ± 0.000005
-99.8	0.999985 ± 0.000005
-119.5	0.999989 ± 0.000005

Only the image region has been irradiated, this may be unrepresentative, since CTE is depending on the read out speed.

The charge passed the image during the frame transfer cycle, which was only 48 μsec per cycle. Therefore the test was repeated at $-80^\circ C$ where the frame transfer was slowed down to simulate the read out time of MONS CCD, 2 $msec$ per cycle. Finally the frame transfer time was increased to match the read out time of the CCD. The CTE measurements were then comparable with those from

the γ -ray irradiation, since the whole CCD was irradiated in that case. In this case the transfer time was set to 14 msec

The results are listed in the table below:

Cycle time (at -80°C)	Parallel CTE
48 μsec	0.999988 \pm 0.000005
2 msec	> 0.999999
14 msec	0.999989 \pm 0.000002

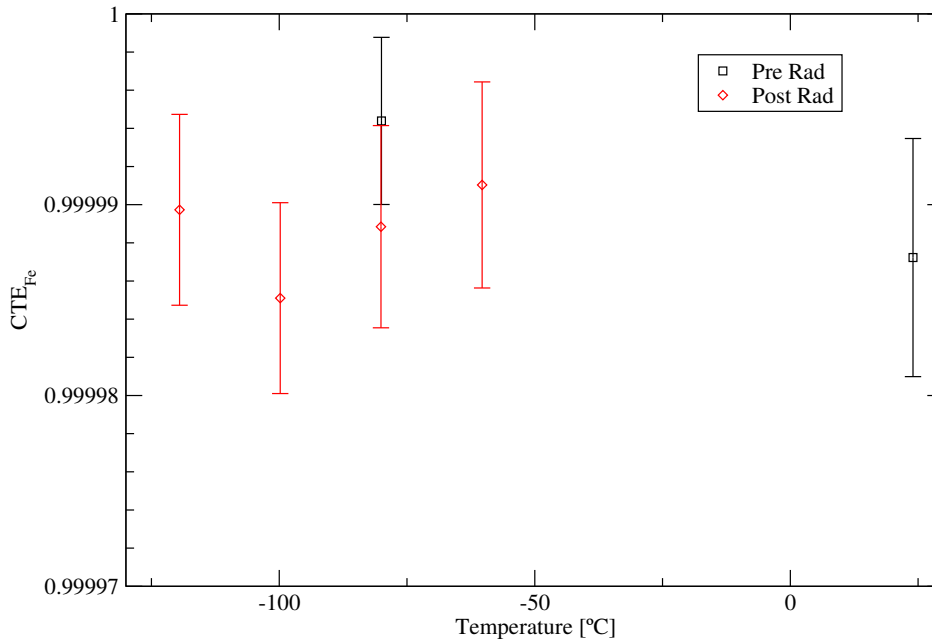


Figure 5.4 CTE performance post radiation is still good.

Chapter VI

Annealing

6.1 Motivation

Annealing describes the effect of the semiconductor to heal itself from damage, in this case caused by radiation.

This chapter deals with the annealing issue, which not really has been mentioned before in this master's thesis. The reason for this is that most defect-annealing will freeze at cryogenic temperatures and thereby become irrelevant. In fact, the most prominent defect type in n-type CCDs is the phosphorous vacancy, which first will anneal at temperatures higher than $+100^{\circ}C$.

However, since the buried n-channel is not a "clean" n-type semiconductor, but rather a p-type which is converted to a n-type by implanting an excess of phosphor atoms into it, interstitial defects and defect complexes associated with boron may arise, some with unknown properties and annealing temperatures. The next section suggests a simple way to treat the annealing issue, based on empirical results. It has not been tested yet, though, whether this is valid in practice.

When components are irradiated by accelerators or other radiation sources for space qualification tests, the dose rate usually is very much higher than the rate the component actually may experience in space. Annealing effects may become important at certain temperatures, where a component may "heal" itself from the radiation effects.

This chapter suggests a way to apply results from radiation testing to a real space application, however, based on some relatively crude estimations. It is merely an idea on how to treat the annealing issue, and has not been checked with real results yet, but could be checked after end of life of the RØMER mission. Also, the suggestion which will be stated in a moment, could be applied for similar devices, such as the RØMER MONS telescope.

6.2 Investigations

Previous proton testing showed that the rise in bulk dark current DC is proportional to the fluence Φ [*protons/cm²*] (e.g. [9]),

$$DC \propto \Phi(T) = \int_0^T \phi(t) dt \quad (6.1)$$

where ϕ is the flux in [*protons/cm²/s*], t is the time in seconds, and T is the total time.

A relatively crude assumption is that all defects N created in the material is the source of bulk dark current, so

$$DC \propto N(t) \quad (6.2)$$

When a component is exposed to the radiation environment in space, new defects will be created with a probability of σ which is the reaction cross-section, thus

$$dN_{\text{generation}} = \sigma\phi(t)dt \quad (6.3)$$

Also some defects are annealing. It is assumed that the annealing process is exponentially decreasing¹, similar to that of a nuclear decay, thus

$$dN_{\text{decay}} = -\lambda N dt \quad (6.4)$$

where λ is the decay constant, i.e. $\lambda = \frac{\ln 2}{T_{1/2}}$, where $T_{1/2}$ is the half life of the defect.

This yields

$$dN = (\sigma\phi(t) - \lambda N)dt \quad (6.5)$$

and when integrating (for $t < T$) we have the general expression:

$$N(T) = \sigma e^{-\lambda T} \int_0^T \phi(t) e^{\lambda t} dt \quad (6.6)$$

However, in practice several defects with different annealing time constants may be present. To simplify things, only three cases are considered:

1. Defects with very short life times, i.e. $T_{1/2} \ll T$, are ignored, since they will evaporate immediately.
2. Defects with very long life times, i.e. $T_{1/2} \gg T$ will not decay during T - this will be added to equation 6.6 shortly.
3. Defects with similar life time to the mission duration, thus $T_{1/2} \simeq T$.

This all comes down to the following general equation:

$$N(T) = \sigma_1 e^{-\lambda T} \int_0^T \phi(t) e^{\lambda t} dt + \sigma_2 \Phi(T) \quad (6.7)$$

where σ_2 is the cross-section for the longterm effects.

Expressed in terms of dark current, it is convenient only to consider the increase in dark current. Two distinct situations are now investigated:

1. The component being irradiated in the laboratory
2. The component suffering from continuous irradiation in orbit over a long time

¹This may be true for some defect types, but not for all.

6.2.1 In the Laboratory

The actual dark current increase $\Delta DC_{lab\ pre-anneal}$ is recorded since the onset of the irradiation until almost immediately after the irradiation², and when annealing has reached a state of equilibrium $\Delta DC_{lab\ post-anneal}$. It is assumed here that the duration of radiation exposure T_{exp} happened in a time scale very much lower than the annealing time constants.

$$\Delta DC_{lab\ pre-anneal} = K_1 \Phi_{lab}(T_{exp}) + K_2 \Phi_{lab}(T_{exp}) \quad (6.8)$$

$$\Delta DC_{lab\ post-anneal} = K_2 \Phi_{lab}(T_{exp}) \quad (6.9)$$

Since the fluence $\Phi_{lab}(T_{exp})$ is known (hopefully!), and the dark current increase can be measured, the constants K_1 and K_2 can be determined.

6.2.2 In Orbit

In orbit, the irradiation never really ceases, and may realistically even vary as a function of time. Eq. 6.7 is rewritten in terms of dark current increase:

$$\Delta DC_{orbit}(t_{orbit}) = K_1 e^{-\lambda t_{orbit}} \int_0^{t_{orbit}} \phi(t) e^{\lambda t} dt + K_2 \Phi(t_{orbit}) \quad (6.10)$$

where t_{orbit} is the elapsed time since orbit insertion.

6.3 Example

A CCD detector is placed into an orbit for $T = 2\ yr = 6.3 \cdot 10^7\ sec$.

The proton flux $\phi(t)$ is assumed to be independent of time, so $\phi = 36\ protons/cm^2/s$ 10 MeV equivalent protons.

Assume the defects anneal with a rate corresponding to $T_{1/2} = 180\ days = 1.6 \cdot 10^7\ sec$.

Furthermore previous testing showed that after many months of irradiation, the component did not degrade further, and the dark current stabilized at approximately 80% of the amount it had immediately after irradiation, which was $\Delta DC_{lab\ pre-anneal} = 1000\ e^-/pixel/s$, thus $\Delta DC_{lab\ post-anneal} = 800\ e^-/pixel/s$. This happened after receiving a fluence corresponding to $\Phi_{lab} = 4 \cdot 10^9\ protons/cm^2$ of 10 MeV equivalent protons. (Do not confuse Φ_{lab} with $\Phi(T_{EOL})$.)

Now the dark current increase at EOL is calculated:

The EOL fluence is:

$$\Phi(T_{EOL}) = 80\ protons/cm^2/s \cdot 6.3 \cdot 10^7\ sec \quad (6.11)$$

$$\Phi(T_{EOL}) \simeq 5 \cdot 10^9\ protons/cm^2 \quad (6.12)$$

and according to eq. 6.8 and eq. 6.9:

²Induced radioactivity and other short term effects may be an issue, but these decay within 15-30 minutes, after irradiation has ceased.

$$K_1 = 5 \cdot 10^{-8} e^- \text{ cm}^2/\text{proton pixel s} \quad (6.13)$$

$$K_2 = 2 \cdot 10^{-7} e^- \text{ cm}^2/\text{proton pixel s} \quad (6.14)$$

The decay constant is found with

$$\lambda = \frac{\ln 2}{T_{1/2}} \quad (6.15)$$

$$\lambda = 4.3 \cdot 10^{-8} \text{ s}^{-1} \quad (6.16)$$

Now the in-orbit equation 6.10 is applied, which is further simplified by the constant fluence:

$$\Delta DC_{orbit}(T_{EOL}) = K_1 e^{-\lambda T_{EOL}} \int_0^{T_{EOL}} \phi(t) e^{\lambda t} dt + K_2 \Phi(T_{EOL}) \quad (6.17)$$

$$\Delta DC_{orbit}(T_{EOL}) = K_1 e^{-\lambda T_{EOL}} \phi \lambda^{-1} (e^{\lambda T_{EOL}} - 1) + K_2 \Phi(T_{EOL}) \quad (6.18)$$

$$\Delta DC_{orbit}(T_{EOL}) = K_1 \phi \lambda^{-1} (1 - e^{-\lambda T_{EOL}}) + K_2 \Phi(T_{EOL}) \quad (6.19)$$

Investigating the useful eq. 6.19 in the limit of $T_{1/2} \rightarrow \infty$ i.e. $\lambda \rightarrow 0$ and doing a first order Taylor expansion (where $e^x \simeq 1 + x$) yields:

$$\Delta DC_{orbit}(T_{EOL}) = K_1 \phi \lambda^{-1} (1 - e^{-\lambda T_{EOL}}) + K_2 \Phi(T_{EOL}) \quad (6.20)$$

$$\Delta DC_{orbit}(T_{EOL}) = K_1 \Phi(T_{EOL}) + K_2 \Phi(T_{EOL}) \quad (6.21)$$

for $\lambda \rightarrow 0$

and

$$\Delta DC_{orbit}(T_{EOL}) = K_2 \Phi(T_{EOL}) \quad (6.22)$$

for $\lambda \rightarrow \infty$

Inserting the figures, the result is:

$$\begin{aligned} \Delta DC_{orbit}(T_{EOL}) &= 5 \cdot 10^{-8} e^- \text{ cm}^2/\text{proton pixel s} \\ &\quad \cdot 80 \text{ protons/cm}^2/\text{s} \cdot (4.3 \cdot 10^{-8} \text{ s}^{-1})^{-1} \\ &\quad \cdot (1 - e^{-4.3 \cdot 10^{-8} \text{ s}^{-1} \cdot 6.3 \cdot 10^7 \text{ s}}) \\ &\quad + 2 \cdot 10^{-7} e^- \text{ cm}^2/\text{proton pixel s} \\ &\quad \cdot 5 \cdot 10^9 \text{ protons/cm}^2 \end{aligned} \quad (6.23)$$

Expressed in terms for both the K_1 and K_2 part (the latter term represents the defects which will not anneal):

$$\Delta DC_{orbit}(T_{EOL}) = 87 e^-/\text{pixel/s} + 1000 e^-/\text{pixel/s} \quad (6.24)$$

in total:

$$= 1087 e^-/\text{pixel/s}$$

If annealing effects would not be taken into account, the result would be:

$$\Delta DC_{orbit}(T_{EOL}) = K_1 \Phi(T_{EOL}) + K_2 \Phi(T_{EOL}) \quad (6.25)$$

thus,

$$\Delta DC_{orbit}(T_{EOL}) = \frac{250e^-}{pixel/s} + \frac{1000e^-}{pixel/s} - \frac{1250e^-}{pixel/s} \quad (6.26)$$

In this case, taking in account annealing effects reduces the predicted amount of damage by 13 %. Whether this is valid in practice, could be investigated in the case of the RØMER satellite.

Chapter VII

Discussion

7.1 Results

First of all neither the gamma ray irradiation nor the proton irradiation caused the CCD to fail operation. The CCD-0 was irradiated with a dose twice as large as the expected ionizing dose the satellite would receive in orbit, but this was absorbed with only little degradation.

The degradation observed caused by **gamma ray irradiation** was:

- A shift in the substrate voltage corresponding to 0.1 ± 0.02 Volts/kRad(Si) due to the hole trapping at the oxide interface.
This matches the expected result stated in the Marconi report [9].
- A significant decrease in the maximum signal level was detected.
This is not associated with the true pixel full well capacity, but rather the saturation of the output amplifier. Apparently the operating point of the amplifier has changed due to the flat-band voltage shift.
- An increase of what is believed to be bulk dark current.
Since also a significant CTE decrease was observed, the only explanation is that the gamma ray energy was so high that it caused a significant amount of displacement damage. Only the presence of bulk damage explain both issues.
A slight increase in the amount of hot pixels have been observed.
- Parallel CTE was degraded by 0.000014 ± 0.000002 at -80°C .

Proton irradiation showed the following degradation:

- Decreased CTE performance.
 $4.05 \cdot 10^9/cm^2$ of 11.5 MeV protons caused a decrease of CTE corresponding to 0.000006 ± 0.000006 at -80°C . The poor standard error arises from the poor signal response of the output FETs on the CCD-1. This results in a degradation factor of $1.48 \cdot 10^{-15} \Delta CTE \text{ cm}^2/p$ at 11.5 MeV. The NIEL for 11.5 MeV protons is approximately $0.00632 \text{ MeV cm}^2/g(\text{Si})$, which then yields a scale factor of $2.34 \cdot 10^{-13} \Delta CTE \text{ g}(\text{Si})/\text{MeV}$. Due to the standard

deviation, this number may be a factor 2 larger (1σ).

According to this the expected CTE degradation will be in the order of 0.000008 since the CTE degradation is proportional with the received fluence of 10 MeV equivalent protons. (Mission fluence / Lab fluence $\cdot \Delta CTE$.)

- Increased bulk dark current.

At $-80^\circ C$ a dark current increase of $6.32 \cdot 10^{-3} e/pix/s$ was expected, due to equation 2.3, assuming $4.05 \cdot 10^9/cm^2$ of 11.5 MeV protons and a depletion volume of $507\mu m^3$ corresponding to a depth of $3 \mu m$.

However, the actual measured dark current increase was over 50 times larger: $0.336 e/pix/s$. The depletion volume is not certain, but can not account for this deviation since the pixel size is well known ($13 \mu m \times 13 \mu m$ and a depletion depth of $156 \mu m$ is unrealistic). Instead the constant in the exponential term, which is associated with the energy level of the defects, is probably set too high. $T^2 \exp(-5852/T)$ seems to fit well. Also the bulk dark current fits in figure 4.8 supports the suggestion of a lower energy constant. This could theoretically be an indication on the presence of other defects than the phosphor-vacancy. But still, the measured dark current was below $1 e^-/pixel/s$, and is therefore insignificantly low.

The amount of hot pixels also remained small at cryogenic temperatures, but a large increase was observed at room temperature.

7.2 Conclusion

For the MONS instrument none of the results imply any problems. Since the CCD detector is being irradiated with a flat field of light and is clocked out with a speed two magnitudes higher than the CTE trapping constant, the existing traps are most likely to be filled immediately, significantly reducing the expected decreases.

Dark current levels are below $1 e/pix/s$ at $-80^\circ C$, and since the integration times for the MONS instrument are below one second, the dark current signal is not identified as a problem. However, there may be a small contribution of noise from the dark current. The noise will mainly arise from hot pixels, and these can readily be “flat fielded out”, if necessary.

Attention should be paid to the flat-band voltage shift, causing the substrate shift. It is recommended to operate the CCD with a minimum of 10 Volts at the substrate potential V_{SS} , which safely will keep the CCD operational for more than 2 years in the Molniya orbit.

The maximum signal level will also decrease with time, but is not expected to decrease to less than $80.000e^-$, which was measured at an ionizing dose corresponding to 4 years in the Molniya orbit during solar minimum.

Thus the conclusion of this thesis is that the Marconi CCD 47-20 backside illuminated CCD may be used as a scientific CCD detector on the MONS telescope, when it is operated at $-80^\circ C$ or lower, as long as the integration- and read

out times are kept short i.e. within the order of seconds.

7.3 Outlook

A secondary task of this master's thesis was to investigate, whether an irradiation facility on the Institute of Physics and Astronomy is possible. During the preparation of this thesis, 3 local accelerators have been considered:

- The 5 MV Van de Graaf accelerator
- The 5 MV Tandem Van de Graaf accelerator
- The storage ring ASTRID at ISA.

7.3.1 5 MV Van de Graaf accelerator

This accelerator is interesting with respect to generate bremsstrahlung, not unlike what is encountered in a satellite structure. However, the fluences were too low, which caused too long irradiation times. It is possible to compensate this by using a direct beam-line, which can perhaps double the rate.

Using the accelerator as a proton irradiation facility may be problematic, since 3 MeV protons only have a range of a few micrometers. This results in a very inhomogeneous energy depletion profile, which is not desirable.

7.3.2 5 MV Tandem Van de Graaf accelerator

This accelerator provides up to 12 MeV protons, and could very well be used for irradiating CCDs and other thin components. The flux is very high by default, running at typically $10^{11} \text{ protons/s cm}^2$, and the beam is narrow by default. Some investments are necessary to solve these issues. Proper dosimetry equipment for lower fluxes, a quadrupole to defocus the beam, reducing the fluence even further and a dedicated vacuum chamber with electrical access are needed.

7.3.3 ASTRID

A synchrotron is not the preferred machine to produce a high energy and moderate fluence proton beam. ASTRID may generate protons up to 150 MeV, but the fluence is very low due to the loss of protons during the acceleration steps. At lower energies, up to 26 MeV, the proton output may in the best case be increased by two decades. But the beam is very small, and widening this up, can easily cost a decade in fluence. However, the CCD irradiated at ASTRID received $4 \cdot 10^9 \text{ protons/s cm}^2$ during 16 hours of operation. A net increase of a decade, reduces this irradiation time to the magnitude of 2 hours, which actually is usable.

Even if these facilities at IFA are not optimal - the most optimal solution would be a super-conducting high-energy cyclotron - the facilities could be used for smaller non-critical irradiation campaigns. The Tandem accelerator and

ASTRID could become relevant in e.g. the ESA Eddington mission, where several CCDs should be radiation tested. But still this requires an one-time-investment in dedicated equipment.

In addition, it should be mentioned here that the European Space Agency have changed their politics regarding radiation hardness and the industry contractors. Instead of providing a list to the industry contractors of components to use, ESA delivers a set of requirements which are to be fulfilled. The industry contractors are thereby left to themselves in terms of device procurement and radiation testing.

In this context it would be an interesting and promising vision to pursue the idea of an irradiation facility at IFA.

Bibliography

- [1] A. Holland, A. Holmes, B. Johlander, and L. Adams, "Techniques for Minimizing Space Proton Damage in Scientific Charge Coupled Devices", *IEEE Trans. Nucl. Sci.*, 38, 1663-1670, 1991.
- [2] Product Assurances & Safety Department and Automation & Informatics Department, European Space Research and Technology Centre Noordwijk, The Netherlands, "The Radiation Design Handbook", ESA PSS-01-609 Issue 1, May 1993.
- [3] C.Dale, P. Marshall, B. Cummings, L. Shameley, and A. Holland, "Displacement Damage Effects in Mixed Particle Environments for Shielded Spacecraft CCDs", *IEEE Trans. on Nucl. Sci.*, Vol. 40, No.6, pp.1628-1637, 1993.
- [4] <http://www.spennis.oma.be/spennis/>
- [5] James Janesick, Tom Elliott, "History And Advancements of Large Area Array Scientific CCD Imagers", *Astronomical CCD Observing and Reduction Techniques*, ASP Conference Series, Vol. 23, 1992, Steve B. Howell, ed.
- [6] Gordon R. Hopkinson, "Space Radiation Effects on CCDs", *Proceedings of the ESA Electronic Components Conference*, ESA SP-313, 301-306, March 1991.
- [7] James Janesick, Tom Elliot, Fred Pool, "Radiation Damage in Scientific Charge-Coupled Devices", *IEEE Trans. Nucl. Sci.*, Vol. 36, No. 1, February 1989.
- [8] James Janesick, George Soli, Tom Elliot, Steward Collins, "The Effects of Proton Damage on Charge-Coupled Devices", *SPIE Vol. 1447*, 87-108, 1991.
- [9] Mark Robbins, "The Radiation Damage Performance of Marconi CCDs", *Marconi Technical Note*, Document: S&C 906/424 Issue 1, February 2000.
- [10] James Janesick, *Scientific Charge Coupled Devices*, SPIE Press monograph; PM 83, ISBN 0-8194-3698-4, (C) 2001 The Society of Photo-Optical Engineering.
- [11] Peter Davidsen, Terma A/S (Birkerød), by correspondance.
- [12] Bjarne Thomsen, Institute of Physics and Astronomy, by correspondance.
- [13] Marconi Applied Technologies, "CCD47-20 Backthinned High Performance AIMO CCD Sensor" Data Sheet, January 2000.

Part III

Appendices

Appendix A

Tables with Stopping Powers and Ranges

A.1 Protons on Aluminium

```

=====
                        SRIM version ---> SRIM-2000.39
                        Calc. date   ---> Mai 13, 2001
=====

```

```

Target = Hydrogen in Aluminum
Density = 2,7020E+00 g/cm3 = 6,0305E+22 atoms/cm3
===== Target Composition =====
  Atom  Atom  Atomic  Mass
  Name  Numb  Percent  Percent
  ----  ----  -
  Al    13    100,00  100,00
=====

```

```

Disk File Name = Hydrogen in Aluminum
Stopping Units = MeV / mm

```

```

Ion = Hydrogen [1] , Mass = 1,008 amu

```

Ion Energy	dE/dx Elec.	dE/dx Nuclear	Projected Range	Longitudinal Stragglng	Lateral Stragglng
1,00 MeV	4,670E+01	3,394E-02	14,30 um	6783 A	8497 A
1,10 MeV	4,403E+01	3,129E-02	16,49 um	7697 A	9580 A
1,20 MeV	4,168E+01	2,905E-02	18,81 um	8616 A	1,07 um
1,30 MeV	3,960E+01	2,713E-02	21,26 um	9543 A	1,19 um
1,40 MeV	3,774E+01	2,546E-02	23,83 um	1,05 um	1,31 um
1,50 MeV	3,606E+01	2,399E-02	26,52 um	1,14 um	1,44 um
1,60 MeV	3,455E+01	2,269E-02	29,34 um	1,24 um	1,58 um
1,70 MeV	3,318E+01	2,154E-02	32,28 um	1,34 um	1,72 um
1,80 MeV	3,192E+01	2,050E-02	35,33 um	1,44 um	1,86 um
2,00 MeV	2,971E+01	1,872E-02	41,79 um	1,76 um	2,16 um
2,25 MeV	2,739E+01	1,690E-02	50,51 um	2,22 um	2,56 um
2,50 MeV	2,545E+01	1,542E-02	59,93 um	2,67 um	2,99 um
2,75 MeV	2,380E+01	1,419E-02	70,04 um	3,10 um	3,45 um
3,00 MeV	2,237E+01	1,316E-02	80,82 um	3,54 um	3,94 um
3,25 MeV	2,113E+01	1,227E-02	92,26 um	3,98 um	4,45 um
3,50 MeV	2,003E+01	1,150E-02	104,36 um	4,42 um	4,98 um
3,75 MeV	1,905E+01	1,082E-02	117,09 um	4,87 um	5,55 um
4,00 MeV	1,818E+01	1,023E-02	130,46 um	5,32 um	6,13 um
4,50 MeV	1,668E+01	9,222E-03	159,05 um	6,87 um	7,38 um
5,00 MeV	1,543E+01	8,405E-03	190,08 um	8,35 um	8,72 um
5,50 MeV	1,437E+01	7,728E-03	223,51 um	9,80 um	10,16 um
6,00 MeV	1,347E+01	7,157E-03	259,29 um	11,24 um	11,68 um

6,50 MeV	1,268E+01	6,668E-03	297,39 um	12,70 um	13,30 um
7,00 MeV	1,199E+01	6,244E-03	337,77 um	14,17 um	15,00 um
8,00 MeV	1,083E+01	5,547E-03	425,16 um	19,25 um	18,67 um
9,00 MeV	9,902E+00	4,996E-03	521,33 um	24,04 um	22,66 um
10,00 MeV	9,131E+00	4,549E-03	626,10 um	28,75 um	26,99 um
11,00 MeV	8,483E+00	4,179E-03	739,29 um	33,45 um	31,63 um
12,00 MeV	7,930E+00	3,867E-03	860,76 um	38,20 um	36,58 um
13,00 MeV	7,451E+00	3,600E-03	990,37 um	43,00 um	41,84 um
14,00 MeV	7,033E+00	3,370E-03	1,13 mm	47,89 um	47,40 um
15,00 MeV	6,664E+00	3,168E-03	1,27 mm	52,86 um	53,25 um
16,00 MeV	6,336E+00	2,990E-03	1,43 mm	57,92 um	59,40 um
17,00 MeV	6,042E+00	2,832E-03	1,59 mm	63,07 um	65,82 um
18,00 MeV	5,776E+00	2,691E-03	1,76 mm	68,31 um	72,53 um
20,00 MeV	5,317E+00	2,448E-03	2,12 mm	86,82 um	86,78 um
22,50 MeV	4,846E+00	2,202E-03	2,61 mm	113,19 um	106,11 um
25,00 MeV	4,460E+00	2,003E-03	3,14 mm	138,37 um	127,09 um
27,50 MeV	4,137E+00	1,838E-03	3,72 mm	163,18 um	149,66 um
30,00 MeV	3,863E+00	1,699E-03	4,35 mm	187,96 um	173,79 um
32,50 MeV	3,627E+00	1,581E-03	5,01 mm	212,91 um	199,44 um
35,00 MeV	3,422E+00	1,478E-03	5,72 mm	238,13 um	226,57 um
37,50 MeV	3,242E+00	1,389E-03	6,47 mm	263,68 um	255,15 um
40,00 MeV	3,082E+00	1,310E-03	7,26 mm	289,60 um	285,15 um
45,00 MeV	2,811E+00	1,178E-03	8,95 mm	381,91 um	349,33 um
50,00 MeV	2,589E+00	1,070E-03	10,80 mm	469,19 um	418,87 um
55,00 MeV	2,405E+00	9,818E-04	12,80 mm	554,57 um	493,58 um
60,00 MeV	2,249E+00	9,072E-04	14,94 mm	639,42 um	573,29 um
65,00 MeV	2,115E+00	8,436E-04	17,22 mm	724,45 um	657,81 um
70,00 MeV	1,999E+00	7,886E-04	19,65 mm	810,03 um	747,01 um
80,00 MeV	1,807E+00	6,983E-04	24,90 mm	1,11 mm	938,86 um
90,00 MeV	1,656E+00	6,272E-04	30,66 mm	1,40 mm	1,15 mm
100,00 MeV	1,532E+00	5,698E-04	36,92 mm	1,67 mm	1,37 mm
110,00 MeV	1,430E+00	5,223E-04	43,66 mm	1,94 mm	1,61 mm
120,00 MeV	1,343E+00	4,824E-04	50,86 mm	2,21 mm	1,87 mm
130,00 MeV	1,269E+00	4,483E-04	58,50 mm	2,49 mm	2,14 mm
140,00 MeV	1,206E+00	4,189E-04	66,56 mm	2,76 mm	2,42 mm
150,00 MeV	1,150E+00	3,933E-04	75,03 mm	3,03 mm	2,71 mm
160,00 MeV	1,101E+00	3,707E-04	83,89 mm	3,31 mm	3,01 mm
170,00 MeV	1,057E+00	3,507E-04	93,14 mm	3,59 mm	3,33 mm
180,00 MeV	1,018E+00	3,328E-04	102,76 mm	3,86 mm	3,66 mm
200,00 MeV	9,513E-01	3,021E-04	123,03 mm	4,87 mm	4,34 mm
225,00 MeV	8,840E-01	2,712E-04	150,23 mm	6,27 mm	5,24 mm
250,00 MeV	8,297E-01	2,461E-04	179,35 mm	7,57 mm	6,19 mm
275,00 MeV	7,852E-01	2,255E-04	210,26 mm	8,81 mm	7,19 mm
300,00 MeV	7,479E-01	2,081E-04	242,81 mm	10,02 mm	8,23 mm

Multiply Stopping by	for Stopping Units
1,0000E-01	eV / Angstrom
1,0000E+00	keV / micron
1,0000E+00	MeV / mm
3,7011E-03	keV / (ug/cm2)
3,7011E-03	MeV / (mg/cm2)
3,7011E+00	keV / (mg/cm2)
1,6582E-01	eV / (1E15 atoms/cm2)
1,0696E-01	L.S.S. reduced units

=====
 (C) 1984,1989,1992,1996,1999 by J.P. Biersack and J.F. Ziegler

A.2 Protons on Tantalum

```

=====
                        SRIM version ---> SRIM-2000.39
                        Calc. date   ---> Mai 13, 2001
=====

Target = Hydrogen in Tantalum
Density = 1,6601E+01 g/cm3 = 5,5248E+22 atoms/cm3
===== Target Composition =====
  Atom  Atom  Atomic  Mass
  Name  Numb  Percent  Percent
  ----  ----  -
  Ta    73    100,00  100,00
=====

Disk File Name = Hydrogen in Tantalum
Stopping Units = MeV / mm

Ion = Hydrogen [1] , Mass = 1,008 amu

  Ion      dE/dx      dE/dx      Projected  Longitudinal  Lateral
  Energy   Elec.      Nuclear    Range      Stragglng     Stragglng
  -----  -----  -----  -----  -----  -----
  1,00 MeV 1,125E+02 1,034E-01 6,11 um    7299 A        1,08 um
  1,10 MeV 1,045E+02 9,590E-02 6,99 um    8023 A        1,21 um
  1,20 MeV 1,007E+02 8,949E-02 7,91 um    8772 A        1,34 um
  1,30 MeV 9,718E+01 8,395E-02 8,87 um    9534 A        1,47 um
  1,40 MeV 9,400E+01 7,911E-02 9,86 um    1,03 um      1,61 um
  1,50 MeV 9,106E+01 7,483E-02 10,89 um   1,11 um      1,75 um
  1,60 MeV 8,835E+01 7,103E-02 11,95 um   1,19 um      1,90 um
  1,70 MeV 8,584E+01 6,763E-02 13,04 um   1,27 um      2,05 um
  1,80 MeV 8,350E+01 6,457E-02 14,17 um   1,35 um      2,20 um
  2,00 MeV 7,928E+01 5,926E-02 16,51 um   1,53 um      2,51 um
  2,25 MeV 7,469E+01 5,381E-02 19,62 um   1,78 um      2,92 um
  2,50 MeV 7,073E+01 4,935E-02 22,92 um   2,02 um      3,34 um
  2,75 MeV 6,725E+01 4,562E-02 26,40 um   2,27 um      3,78 um
  3,00 MeV 6,417E+01 4,245E-02 30,06 um   2,52 um      4,24 um
  3,25 MeV 6,141E+01 3,972E-02 33,89 um   2,78 um      4,71 um
  3,50 MeV 5,893E+01 3,734E-02 37,89 um   3,04 um      5,20 um
  3,75 MeV 5,668E+01 3,525E-02 42,06 um   3,31 um      5,71 um
  4,00 MeV 5,463E+01 3,340E-02 46,40 um   3,58 um      6,23 um
  4,50 MeV 5,101E+01 3,026E-02 55,55 um   4,23 um      7,31 um
  5,00 MeV 4,793E+01 2,769E-02 65,32 um   4,89 um      8,46 um
  5,50 MeV 4,525E+01 2,555E-02 75,72 um   5,56 um      9,65 um
  6,00 MeV 4,290E+01 2,374E-02 86,71 um   6,25 um     10,91 um
  6,50 MeV 4,083E+01 2,218E-02 98,29 um   6,95 um     12,21 um
  7,00 MeV 3,898E+01 2,082E-02 110,45 um  7,67 um     13,57 um
  8,00 MeV 3,580E+01 1,858E-02 136,45 um  9,49 um     16,45 um
  9,00 MeV 3,317E+01 1,680E-02 164,66 um 11,32 um    19,53 um
 10,00 MeV 3,096E+01 1,535E-02 195,02 um 13,19 um    22,80 um
 11,00 MeV 2,906E+01 1,414E-02 227,47 um 15,10 um    26,26 um
 12,00 MeV 2,741E+01 1,312E-02 261,98 um 17,06 um    29,90 um
 13,00 MeV 2,597E+01 1,224E-02 298,50 um 19,08 um    33,73 um
 14,00 MeV 2,469E+01 1,148E-02 337,01 um 21,15 um    37,73 um
 15,00 MeV 2,355E+01 1,082E-02 377,45 um 23,28 um    41,91 um
 16,00 MeV 2,253E+01 1,023E-02 419,81 um 25,47 um    46,25 um
 17,00 MeV 2,160E+01 9,705E-03 464,06 um 27,71 um    50,77 um
 18,00 MeV 2,076E+01 9,234E-03 510,17 um 30,01 um    55,45 um
 20,00 MeV 1,928E+01 8,425E-03 607,83 um 36,06 um    65,29 um

```

22,50 MeV	1,775E+01	7,602E-03	739,94 um	44,42 um	78,49 um
25,00 MeV	1,647E+01	6,933E-03	882,96 um	52,82 um	92,63 um
27,50 MeV	1,539E+01	6,377E-03	1,04 mm	61,36 um	107,70 um
30,00 MeV	1,446E+01	5,908E-03	1,20 mm	70,08 um	123,66 um
32,50 MeV	1,365E+01	5,507E-03	1,37 mm	79,03 um	140,50 um
35,00 MeV	1,295E+01	5,159E-03	1,56 mm	88,20 um	158,18 um
37,50 MeV	1,232E+01	4,855E-03	1,75 mm	97,62 um	176,69 um
40,00 MeV	1,176E+01	4,586E-03	1,96 mm	107,27 um	196,01 um
45,00 MeV	1,081E+01	4,133E-03	2,39 mm	134,21 um	237,03 um
50,00 MeV	1,002E+01	3,765E-03	2,86 mm	160,97 um	281,08 um
55,00 MeV	9,359E+00	3,460E-03	3,37 mm	187,98 um	328,03 um
60,00 MeV	8,794E+00	3,203E-03	3,91 mm	215,45 um	377,79 um
65,00 MeV	8,307E+00	2,983E-03	4,48 mm	243,47 um	430,25 um
70,00 MeV	7,882E+00	2,793E-03	5,09 mm	272,10 um	485,32 um
80,00 MeV	7,174E+00	2,480E-03	6,40 mm	355,08 um	602,94 um
90,00 MeV	6,608E+00	2,233E-03	7,82 mm	436,18 um	730,01 um
100,00 MeV	6,145E+00	2,032E-03	9,37 mm	517,31 um	865,95 um
110,00 MeV	5,758E+00	1,866E-03	11,02 mm	599,26 um	1,01 mm
120,00 MeV	5,430E+00	1,726E-03	12,78 mm	682,43 um	1,16 mm
130,00 MeV	5,148E+00	1,606E-03	14,64 mm	766,98 um	1,32 mm
140,00 MeV	4,904E+00	1,503E-03	16,60 mm	852,97 um	1,49 mm
150,00 MeV	4,689E+00	1,413E-03	18,65 mm	940,42 um	1,66 mm
160,00 MeV	4,500E+00	1,333E-03	20,79 mm	1,03 mm	1,84 mm
170,00 MeV	4,331E+00	1,262E-03	23,02 mm	1,12 mm	2,03 mm
180,00 MeV	4,179E+00	1,199E-03	25,34 mm	1,21 mm	2,22 mm
200,00 MeV	3,919E+00	1,090E-03	30,21 mm	1,48 mm	2,62 mm
225,00 MeV	3,656E+00	9,806E-04	36,72 mm	1,84 mm	3,14 mm
250,00 MeV	3,443E+00	8,916E-04	43,66 mm	2,20 mm	3,69 mm
275,00 MeV	3,267E+00	8,179E-04	51,02 mm	2,54 mm	4,27 mm
300,00 MeV	3,120E+00	7,560E-04	58,74 mm	2,88 mm	4,86 mm

 Multiply Stopping by for Stopping Units

1,0000E-01	eV / Angstrom
1,0000E+00	keV / micron
1,0000E+00	MeV / mm
6,0239E-04	keV / (ug/cm2)
6,0239E-04	MeV / (mg/cm2)
6,0239E-01	keV / (mg/cm2)
1,8100E-01	eV / (1E15 atoms/cm2)
2,2731E-01	L.S.S. reduced units

=====
 (C) 1984,1989,1992,1996,1999 by J.P. Biersack and J.F. Ziegler

A.3 Protons on Silicon

```

=====
                        SRIM version ---> SRIM-2000.39
                        Calc. date   ---> Juni 19, 2001
=====

Target = Hydrogen in Silicon
Density = 2,3212E+00 g/cm3 = 4,9770E+22 atoms/cm3
===== Target Composition =====
  Atom  Atom  Atomic  Mass
  Name  Numb  Percent  Percent
  ----  ----  -
  Si    14    100,00  100,00
=====

Disk File Name = Hydrogen in Silicon
Stopping Units = MeV / (mg/cm2)

Ion = Hydrogen [1] , Mass = 1,008 amu

  Ion      dE/dx      dE/dx      Projected      Longitudinal      Lateral
  Energy   Elec.      Nuclear     Range          Stragglng         Stragglng
  ----    -
500,00 keV 2,691E-01 2,379E-04 5,66 um        3020 A            4147 A
550,00 keV 2,549E-01 2,197E-04 6,47 um        3356 A            4581 A
600,00 keV 2,425E-01 2,043E-04 7,33 um        3697 A            5037 A
650,00 keV 2,314E-01 1,911E-04 8,23 um        4042 A            5514 A
700,00 keV 2,215E-01 1,795E-04 9,18 um        4393 A            6010 A
800,00 keV 2,044E-01 1,604E-04 11,19 um       5485 A            7061 A
900,00 keV 1,902E-01 1,452E-04 13,35 um       6543 A            8185 A
 1,00 MeV 1,781E-01 1,328E-04 15,68 um       7591 A            9379 A
 1,10 MeV 1,657E-01 1,225E-04 18,17 um       8649 A            1,06 um
 1,20 MeV 1,570E-01 1,137E-04 20,82 um       9724 A            1,20 um
 1,30 MeV 1,492E-01 1,062E-04 23,62 um       1,08 um          1,34 um
 1,40 MeV 1,423E-01 9,965E-05 26,56 um       1,19 um          1,49 um
 1,50 MeV 1,361E-01 9,392E-05 29,63 um       1,30 um          1,64 um
 1,60 MeV 1,305E-01 8,886E-05 32,85 um       1,41 um          1,80 um
 1,70 MeV 1,253E-01 8,434E-05 36,19 um       1,53 um          1,96 um
 1,80 MeV 1,207E-01 8,029E-05 39,68 um       1,64 um          2,13 um
 2,00 MeV 1,124E-01 7,331E-05 47,03 um       2,01 um          2,49 um
 2,25 MeV 1,037E-01 6,620E-05 56,95 um       2,54 um          2,96 um
 2,50 MeV 9,644E-02 6,042E-05 67,66 um       3,05 um          3,47 um
 2,75 MeV 9,023E-02 5,562E-05 79,15 um       3,55 um          4,01 um
 3,00 MeV 8,486E-02 5,156E-05 91,39 um       4,05 um          4,59 um
 3,25 MeV 8,018E-02 4,808E-05 104,38 um      4,55 um          5,19 um
 3,50 MeV 7,604E-02 4,507E-05 118,10 um      5,06 um          5,82 um
 3,75 MeV 7,236E-02 4,243E-05 132,55 um      5,57 um          6,48 um
 4,00 MeV 6,906E-02 4,010E-05 147,71 um      6,09 um          7,17 um
 4,50 MeV 6,338E-02 3,616E-05 180,12 um      7,85 um          8,64 um
 5,00 MeV 5,866E-02 3,297E-05 215,28 um      9,53 um          10,22 um
 5,50 MeV 5,466E-02 3,031E-05 253,15 um     11,18 um         11,91 um
 6,00 MeV 5,124E-02 2,807E-05 293,67 um     12,83 um         13,70 um
 6,50 MeV 4,826E-02 2,616E-05 336,80 um     14,48 um         15,60 um
 7,00 MeV 4,564E-02 2,450E-05 382,49 um     16,16 um         17,59 um
 8,00 MeV 4,125E-02 2,177E-05 481,36 um     21,91 um         21,89 um
 9,00 MeV 3,771E-02 1,961E-05 590,13 um     27,35 um         26,58 um
10,00 MeV 3,479E-02 1,786E-05 708,58 um     32,69 um         31,64 um
11,00 MeV 3,233E-02 1,641E-05 836,51 um     38,03 um         37,08 um

```

12,00 MeV	3,023E-02	1,518E-05	973,77 um	43,41 um	42,88 um
13,00 MeV	2,841E-02	1,414E-05	1,12 mm	48,88 um	49,03 um
14,00 MeV	2,682E-02	1,323E-05	1,28 mm	54,43 um	55,53 um
15,00 MeV	2,542E-02	1,244E-05	1,44 mm	60,07 um	62,38 um
16,00 MeV	2,417E-02	1,174E-05	1,61 mm	65,82 um	69,56 um
17,00 MeV	2,305E-02	1,112E-05	1,79 mm	71,68 um	77,07 um
18,00 MeV	2,204E-02	1,057E-05	1,99 mm	77,64 um	84,91 um
20,00 MeV	2,029E-02	9,614E-06	2,39 mm	98,56 um	101,57 um
22,50 MeV	1,850E-02	8,650E-06	2,95 mm	128,35 um	124,15 um
25,00 MeV	1,703E-02	7,868E-06	3,55 mm	156,84 um	148,65 um
27,50 MeV	1,580E-02	7,221E-06	4,20 mm	184,91 um	175,01 um
30,00 MeV	1,476E-02	6,677E-06	4,91 mm	212,97 um	203,18 um
32,50 MeV	1,386E-02	6,212E-06	5,66 mm	241,22 um	233,11 um
35,00 MeV	1,307E-02	5,810E-06	6,45 mm	269,80 um	264,77 um
37,50 MeV	1,238E-02	5,459E-06	7,30 mm	298,75 um	298,13 um
40,00 MeV	1,177E-02	5,150E-06	8,19 mm	328,13 um	333,14 um
45,00 MeV	1,074E-02	4,629E-06	10,10 mm	432,32 um	408,01 um
50,00 MeV	9,895E-03	4,208E-06	12,18 mm	530,91 um	489,13 um
55,00 MeV	9,191E-03	3,859E-06	14,43 mm	627,42 um	576,28 um
60,00 MeV	8,596E-03	3,566E-06	16,85 mm	723,37 um	669,25 um
65,00 MeV	8,085E-03	3,316E-06	19,42 mm	819,57 um	767,83 um
70,00 MeV	7,641E-03	3,100E-06	22,15 mm	916,42 um	871,86 um
80,00 MeV	6,909E-03	2,746E-06	28,07 mm	1,26 mm	1,10 mm
90,00 MeV	6,329E-03	2,467E-06	34,56 mm	1,58 mm	1,34 mm
100,00 MeV	5,857E-03	2,241E-06	41,62 mm	1,89 mm	1,60 mm
110,00 MeV	5,465E-03	2,054E-06	49,21 mm	2,20 mm	1,88 mm
120,00 MeV	5,135E-03	1,897E-06	57,32 mm	2,50 mm	2,18 mm
130,00 MeV	4,853E-03	1,763E-06	65,93 mm	2,81 mm	2,49 mm
140,00 MeV	4,609E-03	1,648E-06	75,01 mm	3,12 mm	2,82 mm
150,00 MeV	4,396E-03	1,547E-06	84,55 mm	3,43 mm	3,16 mm
160,00 MeV	4,208E-03	1,458E-06	94,54 mm	3,74 mm	3,52 mm
170,00 MeV	4,042E-03	1,380E-06	104,96 mm	4,05 mm	3,88 mm
180,00 MeV	3,893E-03	1,309E-06	115,79 mm	4,37 mm	4,26 mm
200,00 MeV	3,637E-03	1,189E-06	138,63 mm	5,50 mm	5,06 mm
225,00 MeV	3,380E-03	1,067E-06	169,27 mm	7,08 mm	6,11 mm
250,00 MeV	3,173E-03	9,685E-07	202,08 mm	8,55 mm	7,22 mm
275,00 MeV	3,002E-03	8,873E-07	236,90 mm	9,95 mm	8,39 mm
300,00 MeV	2,860E-03	8,190E-07	273,57 mm	11,31 mm	9,59 mm

Multiply Stopping by	for Stopping Units
----------------------	--------------------

2,3211E+01	eV / Angstrom
2,3211E+02	keV / micron
2,3211E+02	MeV / mm
1,0000E+00	keV / (ug/cm2)
1,0000E+00	MeV / (mg/cm2)
1,0000E+03	keV / (mg/cm2)
4,6637E+01	eV / (1E15 atoms/cm2)
2,9650E+01	L.S.S. reduced units

=====

(C) 1984,1989,1992,1996,1999 by J.P. Biersack and J.F. Ziegler

A.4 Electrons on Aluminium

The following results were obtained from a figure in “The Atomic Nucleus”, Rob-
ley D. Evans.

Target = Electrons in Aluminum

Density = $2,7020\text{E}+00$ g/cm³ = $6,0305\text{E}+22$ atoms/cm³

Electron Energy	Range in Aluminium	
0,1 MeV	15 mg/ccm	5,6E-03 cm
1 MeV	400 mg/ccm	0,15 cm
2 MeV	1000 mg/ccm	0,37 cm
3 MeV	1500 mg/ccm	0,56 cm
5 MeV	2500 mg/ccm	0,93 cm
7 MeV	3700 mg/ccm	1,37 cm

Appendix B

B.1 CCD Voltages

Main voltage parameters:

PIN	U (V)	Description
V_SS	10.47	Substrate (SS)
V_DD	30.00	FET drain (ODL/ODR)
V_RD	17.00	Reset drain (RDL/RDR)
V_e	3.0	Output gate (OG)

Elsewhere typical values as stated in the Marconi CCD 47-20 data sheet [13] are applied.

B.2 CCD Timing

Standard CCD timing applied during entire testing in this thesis unless stated otherwise:

	Time
Frame transfer cycle	48e-6 sec
Serial cycle	13e-6 sec
Parallel cycle	14e-3 sec

B.3 NIEL Data

These data were kindly provided by Daniel Heynderickx, SPENVIS Project Manager, Belgisch Instituut voor Ruimte Aeronomie, Brussels.

Proton Energy (MeV)	NIEL (MeV cm ² /g(Si))	Equiv 10 MeV flux (/cm ² /s)
0.01	2.0	289.0
0.02	1.3	188.0
0.03	1.0	145.0
0.05	0.69	100.0
0.07	0.54	78.3
0.1	0.41	59.4
0.2	0.24	34.8
0.3	0.17	24.6
0.5	0.11	15.9
0.7	0.085	12.3
1.0	0.063	9.13
2.0	0.032	4.64
3.0	0.022	3.19
5.0	0.014	2.03
7.0	0.0098	1.42
10.0	0.0069	1.00
15.0	0.0054	0.783
20.0	0.0047	0.681
30.0	0.0043	0.623
50.0	0.0037	0.536
70.0	0.0033	0.478
100.0	0.0030	0.435
150.0	0.0025	0.362
200.0	0.0024	0.348
300.0	0.0022	0.319
400.0	0.0021	0.304
500.0	0.0020	0.289
1000.0	0.0017	0.246

B.4 Program Examples

This is a typical example of a shell script which was used for data reduction. It uses commands provided by Bjarne Thomsen's (IFA) IMSYS package.

```
#!/bin/tcsh
# nb_var_list.sh
# LAST CHANGE: 22.07.2002
#
# Extracts dark current variance from dark frames.
#
#
# beware of deferred charge in column 1066 ff...

# some important parameters:
  set bias_first_pixel = 1066
  set bias_last_pixel = 1072

  set output_file_name = ~/temp/dark_var_time_list.dat
  rm $output_file_name

# Extracted viewport: (equals to field which is used by mean,
# ... so make sure bad columns are removed )

# Problem: All dark frames were exposed to light.
# Therefore the shielded columns are used instead.

  set viewport_x_min = 10
  set viewport_x_max = 19
  set viewport_y_min = 1
  set viewport_y_max = 978

# proton part (pre rad):
#   set viewport_x_min = 50
#   set viewport_x_max = 850
#   set viewport_y_min = 50
#   set viewport_y_max = 850

# Building the residual bias frame
echo "Creating residual bias frame..."
foreach i ( `ls bias*.fit` )
  set j = `basename $i .fit`
  echo "  $j"
  rdfits $j
  bias -m-1 $j s$j $bias_first_pixel $bias_last_pixel
  irm $j
  xtract s$j xs$j 2 $viewport_x_min $viewport_x_max $viewport_y_min $viewport_y_max
  irm s$j
end
median -l3 res_bias "xsbias*"
irm "xsbias*"
echo "Done."

# Subtract bias from dark frames,
# and determine variance
echo "Now creating variance dark current list..."
foreach i ( `ls dark*.fit` )
  set j = `basename $i .fit`
```

```
echo -n "  $j"
rdfits $j
bias -m-1 $j s$j $bias_first_pixel $bias_last_pixel
irm $j
xtract s$j xs$j 2 $viewport_x_min $viewport_x_max $viewport_y_min $viewport_y_max
irm s$j
calc xs$j sub res_bias
# mean xs$j > mean_tmp
set meanf = 'mean xs$j | head -1 | awk '{print $9}''

# verbose
mean xs$j

# set meanf = 'get_var mean_tmp'
echo "$meanf" >> $output_file_name
# verbose
echo "  $meanf"
end

# cleanup
irm "xsdark*"
irm res_bias

echo "Done."
echo "Results written to $output_file_name."
echo "Remember to add the exposure times."
```

The next program example is the C-program which was used to compare two frames and extract the amount of hot pixels.

```

/*-----*/
/* This program detects the amount of pixels over a certain      */
/* threshold at the same position in two frames in FITS format.  */
/* bassler@ifa.au.dk                                           */
/*-----*/
/* Version 0.1.3 --- 310702                                     */
/*-----*/
#include <stdio.h>
#include <stdlib.h>
#include <string.h>

#define DETECTION_FACTOR 300.0
#define DETECTION_VAL 25

int get_16bit_integer(FILE *fp);

int main(int argc, char *argv[])
{
    FILE *fp, *fp2;

    long int signed a;
    int n, i, b, b2;
    long int signed mean = 0, total_number_of_pixels = 0;
    float fmean1, limit1;
    float fmean2, limit2;

    /* Count the number of pixels first */

    if ((argc <= 2) || (argc > 3)) {
        printf("usage: fitshotpixel frame1.fit frame2.fit\n");
        exit(1); }
    fp = fopen(argv[1], "r");
    if (fp == NULL) {
        printf("%s: cannot open file.\n", *argv);
        exit(1);
    }
    /* skipping header */
    for (i=0; i < 2880; ++i) {
        a = getc(fp);
    }
    while (getc(fp) != EOF)
        total_number_of_pixels++;
    /* divided by two, since pixels are 2 bytes long */
    total_number_of_pixels /= 2;
    fclose(fp);

    /* ---- FRAME 1 ---- */
    /* Retunerer bare fmean */
    fp = fopen(argv[1], "r");
    if (fp == NULL) {
        printf("%s: cannot open file.\n", argv[1]);
        exit(1);
    }
}

```

```

/* skipping header wich always is 2880 bytes long */
for (i=0; i < 2880; ++i) {
    a = getc(fp);
}
mean = 0;
for (i=0; i < total_number_of_pixels; ++i) {
    b = get_16bit_integer(fp);
    mean += b;
}
fmean1 = (float) mean / total_number_of_pixels;
fclose(fp);
printf("    PIXELS:%.0f\n", (float) total_number_of_pixels);
printf("    Frame 1 MEAN VALUE: %.2f", fmean1);

/* ---- FRAME 2 ---- */
fp = fopen(argv[2],"r");
if (fp == NULL) {
    printf("%s: cannot open file.\n",argv[1]);
    exit(1);
}
/* skipping header */
for (i=0; i < 2880; ++i) {
    a = getc(fp);
}
mean = 0;
for (i=0; i < total_number_of_pixels; ++i) {
    b = get_16bit_integer(fp);
    mean += b;
}
fmean2 = (float) mean / total_number_of_pixels;
fclose(fp);
printf("    Frame 2 MEAN VALUE: %.2f\n", fmean2);

/* Detection algorithm : */
/* limit1 = DETECTION_FACTOR * fmean1;
   limit2 = DETECTION_FACTOR * fmean2;
*/

limit1 = DETECTION_VAL;
limit2 = limit1;

printf("    Frame 1 Limit: %.2f          Frame 2 Limit: %.2f\n", limit1, limit2);

fp = fopen(argv[1],"r");
fp2 = fopen(argv[2],"r");

/* skipping header */
for (i=0; i < 2880; ++i) {
    a = getc(fp);
    a = getc(fp2);
}
n =0;
for (i=0; i < total_number_of_pixels; ++i) {
    b = get_16bit_integer(fp);
    b2 = get_16bit_integer(fp2);
    if ((b > limit1) && (b2 > limit2))
        ++n;
}
fclose(fp);

```

```
fclose(fp2);

printf(" Total amount of pixels detected: %d\n",n);

return(0);
}
```

```
int get_16bit_integer(FILE *fp)
{
    int a;
    char unsigned y;
    char signed x;

    x = getc(fp);
    y = getc(fp);

    /* printf("*** %d %d :",x,y);*/
    /* MSB LSB */
    a = 256 * x + y;

    return a;
}
```

B.5 Abbreviations

ADC	Analog digital converter
ADU	Analog digital units (same as “DN”)
BOL	Beginning of life
CCD	Charge coupled device
Co-60	Cobalt isotope 60
CTE	Charge transfer efficiency
DC	Dark current
DN	Digital number, i.e. ADU
DSNU	Dark signal non-uniformity
DSRI	Danish Space Research Institute
EOL	End of life
ESA	European Space Agency
Fe-55	Iron isotope 55
FET	Field effect transistor
FTP	File transfer protocol
FWC	Full well capacity
GPS	Global positioning system
IFA	Institute of Physics and Astronomy
IJAF	Instrumentcenter for Jordbaseret Astronomisk Forskning
ISA	Institute of Storage Ring Facilities
LED	Light emitting diode
LN2	Liquid nitrogen
MONS	Measuring Oscillations in Nearby Stars
MOS	Metal oxide semiconductor
NIEL	Non-ionizing energy loss
RON	Read out noise
RTS	Random telegraph signal
